Bayesian inference and uncertainty quantification of reduced chemical schemes

J.M. Armengol[a,*], O. Le Maître[b], R. Vicquelin[a]

[a]*Laboratoire EM2C, CNRS, CentraleSupélec, Université Paris-Saclay, Gif-sur-Yvette, France*
[b]*CMAP, CNRS, INRIA, Ecole Polytechnique, 91128 Palaiseau, France*

Abstract

This work concerns the uncertainties arising from the derivation of global chemistry models and their impact on the predictions using modern combustion simulations. We perform the inference of the parameters of a two-step reaction mechanism for CH_4, using synthetic observations of one-dimensional laminar flames generated using detailed mechanism simulations. Introduction of Principal Component Analysis (PCA) and the Polynomial Chaos (PC) expansion, to approximate the global model predictions, enables a full assessment of the inferred global model's posterior. In particular, we employ the Bayesian posteriors' extensive sampling to estimate mean, Maximum a Posteriori, and confidence intervals of the inferred global model's predictions. We contrast the posterior distributions of global quantities of the flame, namely the laminar flame speed, the thermal flame thickness, and the reaction zone thickness, depending on the inference's observations. Finally, we propagate the global chemistry model's posterior distribution through two-dimensional direct numerical simulations (DNS) of a flame-vortex interaction problem. This study highlights the importance of quantifying posterior uncertainties to fully appreciate the impact of using a global model in real-world reactive simulations.

Keywords: Uncertainty quantification, Bayesian inference, Chemistry modeling, Laminar Premixed Flame, Flame-vortex interaction

1. Introduction

Simulation of combustion processes is a complicated and computationally expensive task due to the phenomenon's high dimensionality. A primary concern is to model the chemical kinetics involved in these processes accurately. The accuracy is crucial to predict pollutant formation, flame stabilization, and ignition processes correctly. The most accurate approach to describe the chemical kinetics consists of so-called detailed mechanisms involving many species and elementary reactions. However, numerical simulations of realistic configurations using such mechanisms are, in general, out of reach because of the associated prohibitive CPU costs. The large numbers of intermediate species and reactions, and the small time-steps required to compute intermediate fast reactions accurately, are the principal limitations of detailed mechanisms. Hence, the use of these mechanisms is often limited to 2D simulations of laminar flames [1].

Many efforts are dealing with extending the chemical complexity in 3D computations of turbulent flames by considering either reduced and yet still large mechanisms [2, 3] or recently analytically reduced chemistry [4]. Most flame computations, however, retain much more affordable approaches to include chemical information. Two main strategies are the tabulated chemistry from flamelet archetypes [5] and the global chemistry models [6–9]. The present work focuses on the latter type of models.

Global chemistry models use simplified mechanisms with only a few notable species that interact through a reduced number of global reactions. The global chemistry models are calibrated to match the flame's main

---

*Corresponding author
  Email address: jan.mateu.armengol@gmail.com (J.M. Armengol)

physical features (adiabatic temperature, laminar premixed flame speed, or auto-ignition delay time) in canonical configurations. The early work of Westbrook and Dryer [10] describes a global two-step mechanism for hydrocarbon, reproducing the basic chemical structure, i.e., fast oxidation of the fuel followed by a gradual consumption of the intermediate species. Several works have proposed to improve global mechanisms by adjusting the model parameters of the Arrhenius equations to match laminar burning velocities [11–13]. The adjustment with the equivalence ratio of the pre-exponential constants have been considered more recently [14–16] to improve predictions of the laminar flame speed in the lean and rich regimes simultaneously. Instead of heuristic methods, genetic optimization has been used in several works [17, 18] to systematically set the chemical rate parameters. However, the optimization problem's dimensionality, involving as much as ten model parameters in the Arrhenius equations for a simple two-step scheme, yields a significant amount of uncertainty in the calibration process and the rate parameters. Objective and fair methodologies for assessing global chemistry models uncertainty are then of high interest, and the present work aims to propose such a methodology.

Several works have considered uncertainty quantification (UQ) in reactive flows, mainly for the propagation of Arrhenius parameters uncertainty in detailed chemistry mechanisms, with the objective of its reduction [19–25]. These efforts are crucial to estimate and improve predictions accuracy in these strongly non-linear systems. In this sense, the work of Ji *et al.* [26] characterizes the effects of chemical uncertainties on the lift-off height in a jet flame, through the forward propagation of 21 uncertain rate constants of a detailed mechanism for hydrogen combustion [27]. Other forward propagation studies focus on the uncertainties in the flow, such as in the work of Khalil *et al.* [28], which analyzes the impact of uncertain Smagorinsky coefficient and turbulent Prandtl and Schmidt numbers on the combustion of a methane and hydrogen mixture using a tabulated chemistry model. The authors of [29] and [30] have investigated the effects of uncertain subfilter mixture fraction dissipation rate and chemical kinetic rates, respectively, for the Sandia D Flame partially premixed and using the GRI-Mech 3.0 mechanism [31]. Other references on forward uncertainty propagation are Avdonin *et al.* [32], for the thermoacoustic stability in methane combustion using the two-step reaction mechanism 2S-CM2 [13], and Zhang *et al.* [33], for fuel variability (i.e., uncertain species concentration) effects on the pollutant formation of syngas combustion. Recently, Enderle *et al.* [34] investigated the uncertainties arising from spray boundary conditions specifications in an ethanol flame using detailed chemistry. For a comprehensive review of UQ in combustion systems, we refer to [35, 36]. To our knowledge, uncertainties arising from the derivation of global chemistry models and their impact on the predictions using modern combustion simulations remain to investigate.

The present study thus focuses on the characterization of the calibration uncertainties on the chemical rate parameters of a global chemistry mechanism. To keep the problem tractable, we restrict ourselves to a simple two-step combustion mechanism for methane with constant model parameters. Since these models are only suitable for lean mixtures [16, 37], the present study is limited to the mechanism of lean premixed combustion, i.e., comprising equivalence ratios between 0.6 and 1. With this restriction, the global model has ten uncertain parameters calibrated by a Bayesian inference procedure involving state-of-the-art UQ numerical tools. Specifically, the derivation of the probabilistic global chemistry mechanism and the joint probability density functions of its parameters involve Principal Component Analysis (PCA), Polynomial Chaos (PC) expansion, and the Markov Chain Monte Carlo (MCMC) methods. The uncertain global model is subsequently used to simulate a flame-vortex interaction to assess, in a practical application, the prediction variability and compare it with a detailed mechanism simulation.

The organization of the paper is as follows. The § 2 presents the uncertain prior global model and the one-dimensional laminar premixed flames simulations used for the inference of its parameters. We discuss the construction of the global feature surrogates in § 2.2 and proceed with a brief global sensitivity analysis of the a priori model in § 2.3. The Bayesian inference and the MCMC sampling of the global model posterior are introduced in § 3 and applied on three different cases: (i) calibration based on the flame speed, (ii) calibration based on the flame thermal thickness, (iii) and calibration based on these two global flame quantities simultaneously. Then, § 4 presents the propagation in the flame-vortex simulation of the uncertain global models and, in the light of the results, discusses the adequate methodology to derive global chemistry models. Finally, § 5 summarizes the main results of the work and draws several recommendations for future researches.

2. A priori global model and surrogate

As discussed in the introduction, the Bayesian construction of a probabilistic global model consists of the inference of its parameters to match some characteristic quantities obtained in a reference simulation. The reference considered here consists of laminar flame speed computations using the chemical mechanism GRI 3.0 [31]. The calibration procedure described in § 3 involves the Bayesian update of the prior model parameters distribution, followed by the sampling to the resulting posterior distribution (remaining uncertainty after calibration). In this section, we derive the prior global model, which we subsequently approximate using a Polynomial Chaos (PC) surrogate to alleviate most of the computational burden during the calibration phase. We also use the prior model to perform a global sensitivity analysis of the global model parameters.

2.1. Global model

The global model considers premixed flames as sketched in Fig. 1. The flame front separates the fresh gases, at a low temperature of T_1, from the burnt ones, at a high temperature T_2. The front flame, characterized by a high heat release rate, freely propagates towards the fresh gases at a constant speed S_L (laminar flame speed) with respect to the fresh gases velocity. Throughout the paper, we set the fresh gases' temperature and pressure to 300 K and 1 atm.
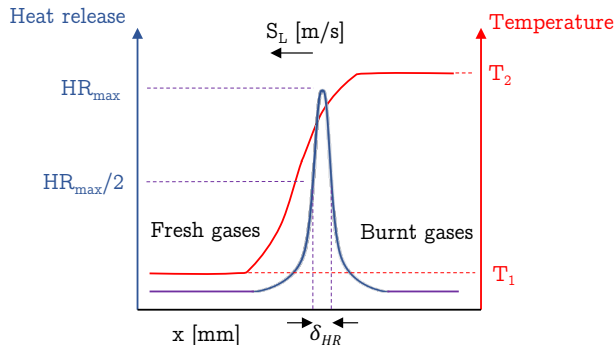

Figure 1: One-dimensional premixed flame scheme. The abscissa corresponds to the propagation axis of the flame. The blue vertical axis (left) corresponds to the heat release rate, while the red vertical axis (right) corresponds to the temperature.

The calibration will concern two types of physical features. The first one is the mentioned flame speed S_L; the second one is the flame thickness, which can have different definitions. The first retained definition uses the reaction zone thickness (δ_{HR}) defined as the distance between the two points in which the heat release equals one half of the maximum heat release value [38], see Fig. 1. Alternatively, the thermal flame thickness δ_T definition combines the temperature difference and maximum gradient through the flame [39]

$$\delta_T = \frac{T_2 - T_1}{\max(|\frac{\partial T}{\partial x}|)}. \tag{1}$$

The global physical quantities have a large dependency on the equivalence ratio ϕ of the mixture, $\phi = \left(\frac{Y_F}{Y_O}\right) / \left(\frac{Y_F}{Y_O}\right)_{st}$, where Y_F and Y_O are the fuel and oxidizer mass fraction, respectively, and $\left(\frac{Y_F}{Y_O}\right)_{st}$ is the stoichiometric proportion between fuel and oxidizer. In this work, we restrict ourselves to the range of equivalent ratios $\phi \in [0.6, 1)$. As further discussed in § 3, the inference of the global model parameters will consider the reference features simulated by the detailed kinetic mechanism GRI 3.0 [31].

The two-step global chemistry model considered for calibration consists of six different species (CH_4, O_2, CO, H_2O, CO_2 and N_2) and two reactions. The first is an irreversible reaction,

$$CH_4 + \frac{3}{2}O_2 \rightarrow CO + 2H_2O, \tag{2}$$

3

and the second is a reversible reaction that leads to an equilibrium between CO and CO_2 in the burnt gases:

$$CO + \frac{1}{2}O_2 \Leftrightarrow CO_2. \tag{3}$$

The reaction rates of the two reactions are modelled by a modified Arrhenius law as

$$k_1 = A_1 T^{\beta_1} [CH_4]^{n_{CH_4}} [O_2]^{n_{O_2,1}} e^{-E_{a,1}/RT}, \tag{4}$$

and

$$k_2 = A_2 T^{\beta_2} [CO]^{n_{CO}} [O_2]^{n_{O_2,2}} e^{-E_{a,2}/RT}, \tag{5}$$

with $[X]$ the molar concentration corresponding to the species X. Other physical coefficients of the flame problem include the heat diffusion coefficient, which is set assuming a constant Prandtl number $\mathrm{Pr} = 0.7$, and a power law model for the molecular viscosity following the expression $\mu = \mu_0 \left(\frac{T}{T_n}\right)^n$ where $\mu_0 = 1.807 \times 10^{-5}$ Pa·s, $T_n = 300$ K and $n = 0.682$. The mixture viscosity also determines the species diffusion coefficient through the Schmidt number of each species reported in Table 1.

Table 1: Schmidt numbers of the considered species.

CH_4	CO_2	CO	O_2	H_2O	N_2
0.677	0.945	0.750	0.739	0.544	0.726

The uncertain parameters of the global model are then the 10 coefficients A_1, A_2, β_1, β_2, n_{CH_4}, $n_{O_2,1}$, n_{CO}, $n_{O_2,2}$, $E_{a,1}$ and $E_{a,2}$ of the reaction rates in Eqs. 4 and 5. Regarding the prior distributions of these parameters, we assume that they are independent, a priori, and follow log-normal distributions, except for β_1 and β_2, which are equipped with uniform distributions. For a generic random rate parameter θ_i with log-normal distribution, we denote $\bar{\theta}_i$ its nominal value and $UF_i \geq 1$ its uncertainty factor. The log-normal distribution of θ_i is imposed by introducing a canonical random variable ξ_i with standard Gaussian distribution, $\xi_i \sim \mathcal{N}(0, 1)$, and setting

$$\theta_i = \bar{\theta}_i \exp\left(\frac{\xi_i}{3} \ln(UF_i)\right). \tag{6}$$

As a result of the canonical representation in (6), θ_i has a median value $\bar{\theta}_i$ and $\approx 99.9\%$ probability to be in the interval $[\bar{\theta}_i/UF_i, \bar{\theta}_i UF_i]$. In the case of θ_i having a uniform distribution (β_1 and β_2) with range $[a, b]$, we consider a uniform canonical random variable $\xi_i \sim \mathcal{U}(0, 1)$ and set

$$\theta_i = a + (b - a)\xi_i. \tag{7}$$

The nominal values of the log-normal parameter are taken from the 2-step scheme 2sCM2 [13] and slightly modified to account for non-zero β_i parameters. We select the uncertainty factors to ensure a wide range of flame speeds and thicknesses while remaining within the convergence (stability) domain of the one-dimensional premixed flame simulations. Table 2 summarizes the prior distributions of the global model parameter. The resulting variability of flame speed and thicknesses in the global 2-step mechanisms can be appreciated from Figure 2. The curves correspond to a sample set of $N_s = 10,000$ realizations of the global model generated by a Quasi-Monte Carlo (QMC) method based on a low-discrepancy Sobol sequence [40]. For each realization, the one-dimensional laminar premixed flames are computed for several equivalence ratios in the range $[0.6, 1)$ with mesh adaptation using the EM2C in-house solver Agath. The figure also reports the laminar flame speeds and thicknesses predicted with the detailed chemistry model, which are within the a priori uncertainty range.

4

Table 2: Prior distributions of the global model parameters. Parameters in the first row are in SI except for the activation energies ($E_{a,i}$) in cal/mol. Pre-exponential factors (A_i) are in cgs units in the second row.

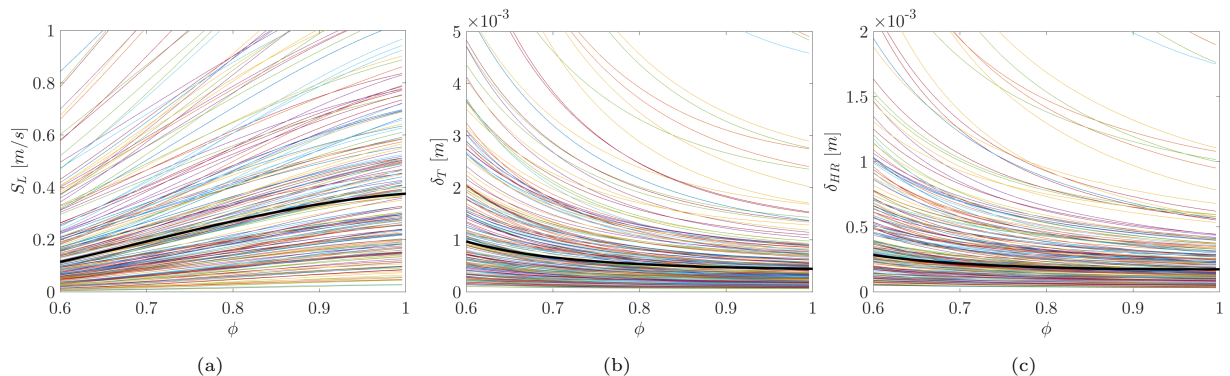|	A_1	β_1	n_{CH_4}	$n_{O_2,1}$	$E_{a,1}$	A_2	β_2	$n_{O_2,2}$	n_{CO}	$E_{a,2}$
$\bar{\theta}_i$	2×10^9	$\sim \mathcal{U}(0, 1/2)$	0.9	1.1	4.1727×10^4	2×10^6	$\sim \mathcal{U}(0, 1)$	0.5	1.0	1.2916×10^4
(cgs)	2×10^{15}					2×10^9				
UF_i	1.5	-	1.5	1.5	1.5	1.5	-	1.5	1.5	1.5

(a) (b) (c)

Figure 2: A priori QMC samples of the a priori global model as functions of the equivalent ratio ϕ: (a) laminar flame speed, (b) laminar flame thermal thickness, and (c) laminar flame thickness based on heat release rate. In thick solid black line: the laminar flame speed and thicknesses for the detailed chemistry model discussed in § 3.

2.2. Surrogate model

A surrogate model for 2-step mechanisms is constructed to accelerate the Bayesian inference; to this end, N_s samples of the a priori model are generated by randomly varying the model parameters. Denoting by v any of the global features (S_L, δ_T and δ_{HR}), we construct a surrogate model for $v(\phi, \boldsymbol{\xi})$ where $\boldsymbol{\xi}$ is the set of canonical random variables previously introduced.

We start by introducing a grid of $N_\phi = 51$ equivalent ratio values to discretize the dependence of the feature $v(\phi, \boldsymbol{\xi})$ on equivalent ration ϕ, and we denote $\boldsymbol{v}(\boldsymbol{\xi})$ the random feature vector at the discrete ϕ values:

$$\boldsymbol{v}(\boldsymbol{\xi}) = \left(v(\phi_1, \boldsymbol{\xi}) \cdots v(\phi_{N_\phi}, \boldsymbol{\xi}) \right)^\top .$$

Further, let us denote $\boldsymbol{v}^i \doteq \boldsymbol{v}(\boldsymbol{\xi}^i)$ the vector of feature associated to the i-th realization of the canonical random variables.

In the first stage, a Principal Component Analysis (PCA), also called Proper Orthogonal Decomposition (POD), is applied independently on the global features S_L, δ_T, and δ_{HR}. The objective is to reduce N_ϕ to a lower value, N_{red}, by exploiting the smoothness of each realization. It is worth mentioning that the PCA is applied to preconditioned data, using a logarithmic transformation designed to enforce almost sure positivity for the reduced model. The Appendix Appendix A details the preconditioned PCA method. The number of reduced modes needed to represent the dependencies on ϕ depends on the desired accuracy and the behaviour of the global physical feature on which the dimensionality reduction is applied. In the present case, $N_{red} = 4$ for the flame speed and $N_{red} = 3$ for flame thickness based on both temperature and heat release were enough to achieve a relative error of less than 0.1%. With this reduction, the random feature vector is approximated by

$$\boldsymbol{v}(\boldsymbol{\xi}) \approx \exp \left[\sum_{r=1}^{r=N_{red}} \boldsymbol{l}_r a_r(\boldsymbol{\xi}) \right], \tag{8}$$

where $N_{red} \ll N_\phi$ and the exponential applies component-wise to vectors.

In the second stage, the dependences on the canonical random variables $\boldsymbol{\xi}$ of the vector of reduced

5

coordinates $\boldsymbol{a}(\boldsymbol{\xi}) \doteq (a_1(\boldsymbol{\xi}) \cdots a_{N_{red}}(\boldsymbol{\xi}))^{\top}$ is sought as a PC expansion [41, 42],

$$\boldsymbol{a}(\boldsymbol{\xi}) \approx \sum_{\alpha=1}^{\alpha=N_{pol}} \boldsymbol{a}_\alpha \Psi_\alpha(\boldsymbol{\xi}), \tag{9}$$

where the vectors $\boldsymbol{a}_\alpha$ are the PC coefficients of the reduced coordinates and the Ψ_α form an orthonormal family of multi-variate polynomials in the random canonical variables. The PC expansion is truncated at a prescribed polynomial degree selected to control the truncation error. For the practical determination of the PC coefficients, we proceed with an ordinary least squares method using the N_s samples available; see Appendix Appendix B for more details.

Inserting the PC expansion of the reduced coordinates, we obtain the final form of the surrogate of the random feature vector:

$$\boldsymbol{v}(\boldsymbol{\xi}) \approx \exp\left[\sum_{\alpha=1}^{\alpha=N_{pol}} [L]\boldsymbol{a}_\alpha \Psi_\alpha(\boldsymbol{\xi}) \right] \doteq \boldsymbol{v}_{PC}(\boldsymbol{\xi}), \tag{10}$$

where $[L] \doteq [\boldsymbol{l}_1 \cdots \boldsymbol{l}_{N_{red}}]$ is the matrix of PCA modes.

In the present work, the PC expansion uses a total degree truncation of order 4. As the global model employs a total of $N_{dim} = 10$ canonical random variable $\boldsymbol{\xi}$, the PC basis has $N_{pol} = 1001$ polynomials Ψ_α. We rely on the sample set of $N_s = 10^4$ realizations $\boldsymbol{v}^i$ for the construction. Therefore we have roughly ten times more realizations than PC coefficients to compute, and we found it unnecessary to use an adaptive PC expansion strategy.

The accuracy of the surrogate models of the features have been carefully assessed by relying on an auxiliary validation set of 2×10^3 realizations. The details of the validation are not shown here and we simply report the estimated normalized mean squared error,

$$\epsilon_{rel}^2 = \frac{\mathbb{E}\left[\|\boldsymbol{v}(\boldsymbol{\xi}) - \boldsymbol{v}_{PC}(\boldsymbol{\xi})\|^2\right]}{\mathbb{E}\left[\|\boldsymbol{v}(\boldsymbol{\xi})\|^2\right]}. \tag{11}$$

For the fourth-order PC expansion, we obtained $\epsilon_{rel} = 1.44\%$ for the thermal flame thickness, 1.94% for the reaction zone thickness and 1.97% for the flame speed. The accuracy of the approximation is easier to appreciate in Fig. 3 which compares some global model features with their surrogate approximations for several parameter values not included in the training set. We observe a generally excellent agreement, which tends to degrade for the most extreme realizations.
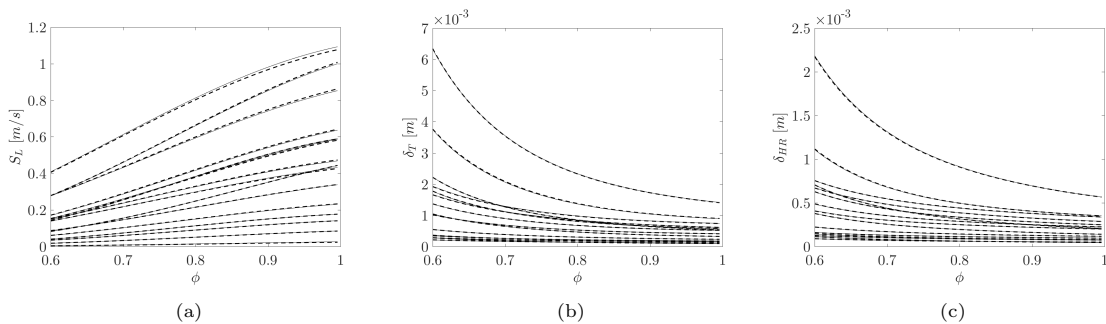

Figure 3: Comparison of the model features (dashes line) and their surrogate approximation (continuous line): Flame velocity (a), thermal flame thickness (b), and reaction zone thickness (c).

2.3. A priori sensitivity analysis

The surrogate models of the global features of the random model provide a fast, accurate, and inexpensive way to predict the flame velocity and thicknesses for any value of the canonical random variables in their

a priori range and any equivalent ratio value $\phi \in [0.6, 1)$ (through interpolation over the components of $\boldsymbol{v}_{PC}(\boldsymbol{\xi})$). The surrogates are exploited in the calibration stage to sample the posterior distribution during the Bayesian inference process.

Before engaging in the calibration, we propose to complete this section on the prior model by performing a brief global sensitivity analysis to assess the relative influence of each model parameter on the flame features (S_L, δ_T and δ_{HR}). To this end, we take advantage of the PC surrogate to compute the Sobol indexes [43] corresponding to the decomposition of the variance of $\boldsymbol{v}_{PC}(\boldsymbol{\xi})$. Precisely, for each discretized value ϕ_i of the equivalent ratio, we compute the first and total order sensitivity indices of $v_i(\boldsymbol{\xi})$. The first-order indices correspond to the fraction of variance induced by the considered parameter and this parameter only, while the total order indices account for the fraction of variance attributed to the parameter and its interactions with others. We only report below the case of the flame speed S_L, the other global features (thicknesses) presenting similar sensitivities. Figures 4a and 4b show the first-order indexes for the parameters of the first and second reactions, respectively. We see that the dominant individual effects on the flame speed are due to parameters $E_{a,1}$ and β_1 of the first reaction, whose cumulated single effects tops to close to 80% of the variance, when the single effects of the second reaction sum-up to less than 2% of the variance. The total sensitivity indices, shown in Figs. 4c and 4d, confirm the dominance of $E_{a,1}$ and β_1 on the flame speed variability, although β_2 is seen to play a significant role through its interactions. The effects of the second reaction parameters appear to be limited to interactions with the first reaction parameters. Also, the sum of the total indices significantly exceeds 1, underlying high interactions between parameters and non-additive effects. This analysis is instructive because we can anticipate that parameters having low to negligible effects on the global features will be harder to calibrate from these quantities. In contrast, parameters strongly affecting the features should be well-informed by the calibration data.
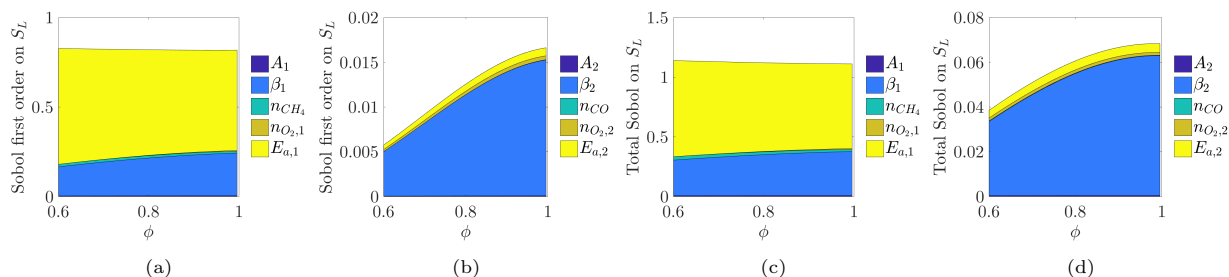

Figure 4: Sobol indices of first (a,b) and total (c,d) orders for the laminar flame speed, associated to the first (a,c) and second (b,d) chemical reaction parameters.

3. Global scheme calibration results using Bayesian inference

This section concerns the calibration of the two-step mechanism for CH_4. The calibration takes advantage of the surrogate models to approximate the flame speeds and thicknesses over the range of equivalent ratios and prior range of the global mechanism's parameters. To illustrate the Bayesian calibration methodology, its capabilities, and limitations, we perform three inference exercises. The first inference uses flame speed observations only; the second inference considers thermal thickness observations; finally, the third inference problem included flame speed and thermal thickness observations. The three inferences lead to three reduced models differing by the posterior distribution of their parameters. We also contrast the results obtained for two values of the observation noise in the last inference.

In the Bayesian inference framework, the model parameters are regarded as random variables rather than fixed quantities. Then, the main objective is to obtain posterior distributions for the model parameters and derive relevant information, such as the most likely values (Maximum A Posteriori, MAP), their variability (variance), possible correlations, estimated density, . . . Besides the distribution of the parameters, one is usually interested in the characterization of the model's predictive posterior. This predictive posterior can

be assessed by sampling the parameters' posterior and solve the forward propagation problem to measure the resulting uncertainty in various quantities of interest, *e.g.*, in situations differing from the calibration setup. This latter point is the focus of the next section.

The parameters' posterior is not obtained as a closed-form expression, and its sampling requires appropriate methods. We rely on a Markov Chain Monte Carlo (MCMC) method to generate samples from the posterior probability distribution function in this work. The MCMC algorithm randomly generates a sequence of samples (states), where the next state of the chain is conditioned on the current state, creating a so-called Markov chain. With a suitable probabilistic transition rule from a state to the next, the random chain converges to the target distribution as the number of steps increases. Different MCMC algorithms are available. In this study, we use the Metropolis-Hasting algorithm [44] to draw samples from the posterior. We outline this algorithm in Appendix Appendix C. For convenience, the posterior is expressed in terms of the random vector of canonical variables $\boldsymbol{\xi}$, as $p(\boldsymbol{\xi}\,|\,\boldsymbol{v}^{obs})$ with $\boldsymbol{v}^{obs}$ the vector of observations used for the calibration. Using the Bayes Theorem, the posterior is proportional to the product of the prior distributions $\pi_\xi(\boldsymbol{\xi})$ with the likelihood of the observations,

$$p\left(\boldsymbol{\xi}\,|\,\boldsymbol{v}^{obs}\right) \propto \mathcal{L}\left(\boldsymbol{v}^{obs}\,|\,\boldsymbol{\xi}\right)\pi_\xi\left(\boldsymbol{\xi}\right). \tag{12}$$

Details on the posterior distribution derivation and the sampling procedure can be found in Appendix Appendix C.

The vector of observations is derived from simulations based on the detailed kinetic mechanisms GRI 3.0 [31], which involves 53 species and 325 reactions. Figure 5 shows the flame speed (S_L) and the thermal flame thickness (δ_T) simulated with the detailed kinetic mechanisms, together with experimental values of Akram *et al.* [45], Liu and Kim [46] and Lafay *et al.* [47], and numerical results of Mazas *et al.* [48].
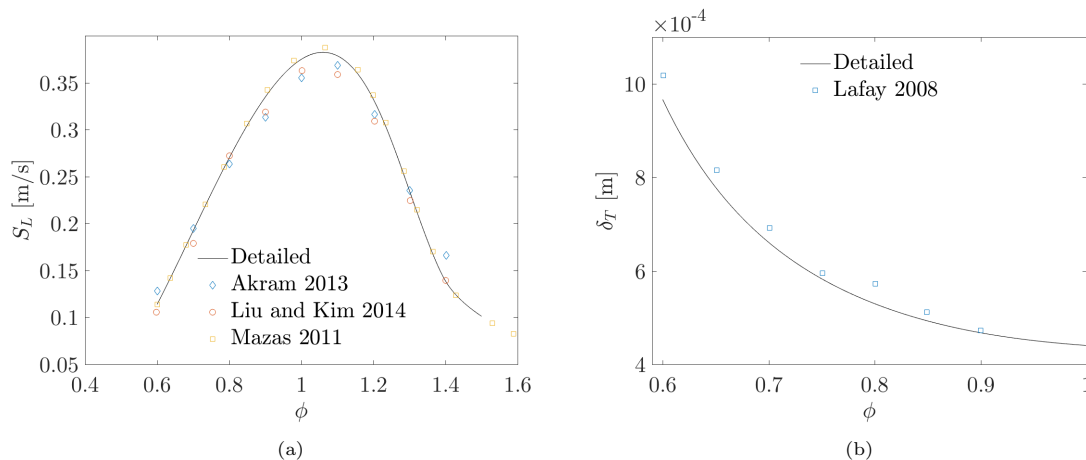

Figure 5: One-dimensional premixed flame results using GRI 3.0 [31] detailed chemistry. (a) Comparison of the computed flame speed with experimental results (Akram *et al.* [45], Liu and Kim [46]) and numerical (Mazas *et al.* [48]) studies. (b) Computed thermal flame thickness compared with experimental data of Lafay *et al.* [47].

3.1. Calibration based on flame speed observations

We first perform the Bayesian inference of the model parameters using flame speed observations only. To this end, we need to define the likelihood function that prescribes the discrepancy between the observations and the reduced model predictions. In our situation, the discrepancy results primarily from the reduction error, which is dependent on ϕ, and, possibly, some numerical error in the model's evaluation. The latter error is negligible. To avoid proposing and identifying a perhaps complex statistical model for the reduction error, we instead corrupt the detailed model predictions with a centered Gaussian noise. The noise variance $\sigma^2_{\epsilon,S_L} > 0$ is selected to dominate the reduction error. In these conditions, a classical independent Gaussian

discrepancy model is suitable, leading to the following likelihood

$$\mathcal{L}_{S_L}\left(\boldsymbol{S}_{\mathrm{L}}{}^{obs}\left|\boldsymbol{\xi},\sigma^2_{\epsilon,S_L}\right.\right) = \frac{1}{\sqrt{(2\pi\sigma^2_{\epsilon,S_L})^{N_\phi}}}\exp\left[-\frac{\left\|Y_{S_L}\left(\boldsymbol{\xi}\right)-\boldsymbol{S}_{\mathrm{L}}{}^{obs}\right\|^2}{2\sigma^2_{\epsilon,S_L}}\right], \tag{13}$$

where $Y_{S_L}\left(\boldsymbol{\xi}\right)$ is the PC expansion approximation of the vector of predicted flame speeds, function of $\boldsymbol{\xi}$; and $\boldsymbol{S}_{\mathrm{L}}$ is the vector of observed flame speeds whose components are independently corrupted by adding a random perturbation drawn from the normal distribution $N(0, \sigma^2_{\epsilon,S_L})$. Larger values of σ^2_{ϵ,S_L} allows for larger discrepancies and produces a flatter posterior, as deviations from $\boldsymbol{S}_{\mathrm{L}}$ are less penalized. In contrast, a low value of σ^2_{ϵ,S_L} leads to a tight posterior around the parameters maximizing the likelihood and prior product. In the latter case, the inference can produce unsatisfying models, corresponding to extreme parameter values ensuring the "best fit," lacking robustness, and overly confident (low variability) posterior predictions not reflecting the inferred model's actual predictive capability. After several tests, we selected a value of σ_{ϵ,S_L} equal to 10 % of S_L at $\phi = 0.8$. This value is consistent with the amount of noise in the experimental data reported in Fig. 5 and provides robust inference results. The consequences of using smaller values of σ_{ϵ,S_L} are addressed in the last part of § 3.3.

To characterize the posterior distribution of the model parameters, defined by Eqs. (12) and (13), we run a MCMC chain with 10^7 steps thanks to the low evaluation cost achieved by the PC approximation. A burn-in period of 10^6 steps is first performed to converge to the stationary distribution before recording the samples. The resulting sample set is eventually post-treated to estimate the posterior statistics, such as the parameters' marginal distribution.

Figure 6 compares the prior and posterior marginal distributions of the reduced model parameters. The plots show that the posterior marginals of A_1, A_2, $n_{O_2,2}$, n_{CO} and $E_{a,2}$ remain close to their respective priors, implying that the observations do not inform these parameters of the flame speed. These low progress were anticipated in § 2.3, in which we have shown that these parameters have not a significant impact on the flame speed. Consistently, we observe more significant differences in the prior and marginal of the two most sensitive parameters, namely $E_{a,1}$ and β_1, indicating an information gain after inference and a better knowledge a posteriori of these parameters.
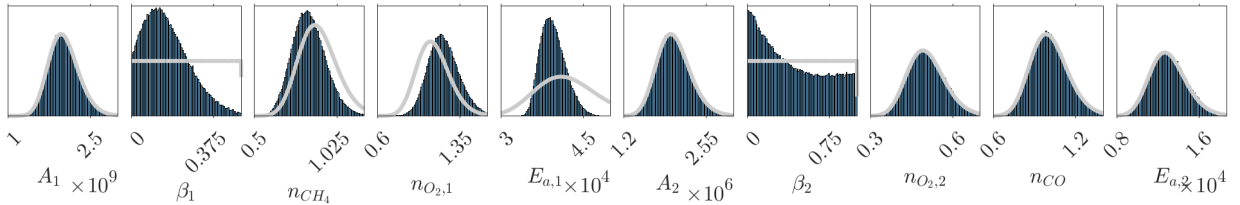

Figure 6: Prior and posterior marginals of the model parameters for the thermal flame speed calibration.

Table 3 reports the maximum a posteriori (MAP) values of the parameters, maximizing the posterior distribution. Besides this "best-fit" value, it is important to stress that the calibration not only identifies the MAP values but also provides a complete probabilistic description of the parameters' joint-posterior. Among other statistics, this detailed information enables the estimation of the posterior parameters variance, correlations or credibility intervals.

Table 3: MAP values of the model parameters for the flame speed calibration. The values in the second row are in SI units, except for the activation energies ($E_{a,i}$) in cal/mol. Pre-exponential factors (A_i) in the third row are in cgs units.

A_1	β_1	n_{CH_4}	$n_{O_2,1}$	$E_{a,1}$	A_2	β_2	$n_{O_2,2}$	n_{CO}	$E_{a,2}$
2.0822×10^9	0.2068	0.8858	1.1492	3.9934×10^4	1.8928×10^6	0.0694	0.4977	1.0157	1.3329×10^4
3.3769×10^{15} in cgs					2.2777×10^9 in cgs				

Perhaps more important than the complete knowledge of the parameters' posterior distribution is the possibility to assess the predictive capabilities of the model with its posterior uncertainty. As an illustration, we report in Fig. 7 the posterior predictions of the reduced model for the laminar flame speed (Fig. 7a), flame thermal thickness (Fig. 7b), and reaction zone thickness (Fig. 7c). Specifically, we report the posterior means with ± 3 standard deviation range (shaded areas) to assess the posterior uncertainty level and the reference solution based on the detailed mechanism. The flame speed plot also shows the observations used in the inference. The mean and standard deviation estimates use a large sample set of parameters drawn from the posterior distribution with the Markov Chain and the PC approximation constructed in § 2.2 of the flame's speed and thicknesses. For verification, we also provide the reduced model solutions for the MAP value of the parameters (black lines) reported in table 3. Focusing first on the flame speed in Fig. 7a, we observe a dramatic reduction of the spread of the predicted flame speed compared to the a priori situation shown in Fig. 2. The posterior mean and MAP predictions of the flame speed are also in excellent agreement with the reference solution, which falls well within the uncertainty range. A critical reduction of the prediction variance for the flame thickness is also visible in Fig. 7b, with limited $\pm 3\sigma$ areas. However, the reference solution is not within the posterior uncertainty range. Analysis of the reaction zone thickness results, in Fig. 7c, yields similar conclusions. However, the predictions agree better with the reference, mainly because of the generally more extensive posterior uncertainty range than for the flame thickness. From this inference experiment, one can conclude that the model's calibration on flame speed observations provides a reduced model somewhat effective at predicting this quantity (and with low posterior uncertainty), but having the limited capability for the other features.
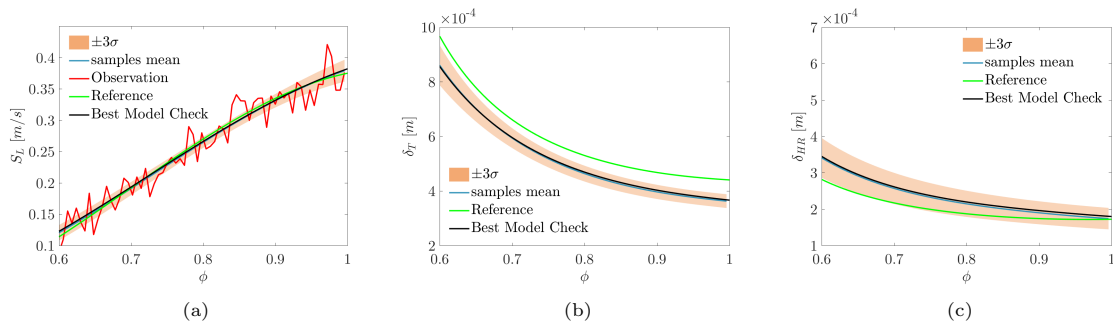

Figure 7: A posteriori predictions of (a) flame speed, (b) thermal flame thickness and (c) reaction zone thickness compared with the detailed kinetic mechanism (Reference). Case of the flame speed calibration.

3.2. Calibration based on the thermal flame thickness

Following the calibration on flame speed observations, we now consider the calibration from flame thickness noisy observations. The noise level $\sigma_{\epsilon, \delta_T}$ used to corrupt the detailed model computations is again set to 10% of δ_T at $\phi = 0.8$, and the likelihood function becomes

$$\mathcal{L}_{\delta_T}\left(\boldsymbol{\delta}_{\mathrm{T}}^{obs}\left|\boldsymbol{\xi}, \sigma_{\epsilon, \delta_T}^2\right.\right) = \frac{1}{\sqrt{(2\pi\sigma_{\epsilon, \delta_T}^2)^{N_\phi}}} \exp\left[-\frac{\left\|Y_{\delta_T}\left(\boldsymbol{\xi}\right) - \boldsymbol{\delta}_{\mathrm{T}}^{obs}\right\|^2}{2\sigma_{\epsilon, \delta_T}^2}\right]. \tag{14}$$

Following the same MCMC sampling procedure used for the flame thickness calibration, Fig. 8 compares the prior and posterior marginals of the model parameters. Again, the parameters β_1 and $E_{a,1}$ are the two parameters the most informed by the observations. Overall, the posterior marginals look very close to their counterparts in Fig. 6.

Table 4 list the MAP parameters for the flame thickness calibration. Comparing these values with the MAP of the flame speed calibration in Table 3 large differences emerge for the coefficients β_1 and β_2, and smaller ones for the n_{CH_4}, $n_{O_2,1}$ and n_{CO}, while differences in the remaining MAP parameters are less than 1%.
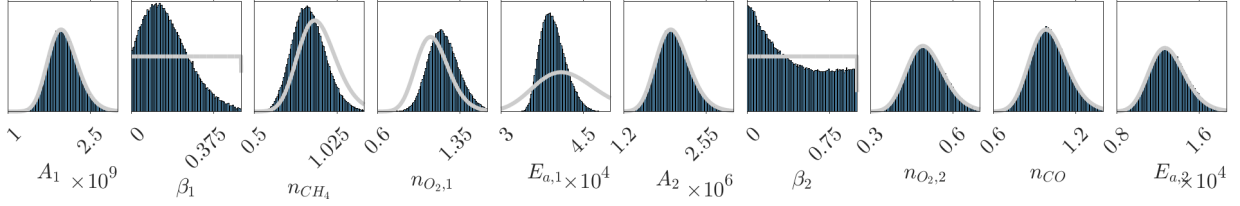
Figure 8: Prior and posterior marginals of the model parameters for the thermal flame thickness calibration.

Table 4: MAP values of the model parameters for the flame thickness calibration. The values in the second row are in SI units, except for the activation energies ($E_{a,i}$) in cal/mol. Pre-exponential factors (A_i) in the third row are in cgs units.

A_1	β_1	n_{CH_4}	$n_{O_2,1}$	$E_{a,1}$	A_2	β_2	$n_{O_2,2}$	n_{CO}	$E_{a,2}$
2.0104×10^9	0.0896	0.7761	1.2112	3.9193×10^4	2.0230×10^6	0.1735	0.5059	0.9341	1.3022×10^4
1.6869×10^{15} in cgs					8.8307×10^8 in cgs				

To appreciate the effect of calibrating the model on flame thickness observations, Fig. 9 presents the posterior prediction of the flame global features S_L, δ_T and δ_{HR}. The generation of the plots follows the same methodology as previously. As for the calibration on flame speed observations, the predictions' uncertainty reduces a lot from the a priori. However, in contrast with the results shown in Fig. 7, the prediction of the flame thickness is now in excellent agreement with the reference, while the flame speed prediction significantly deteriorates, systematically underestimating S_L by a margin large compared to the ± 3 standard deviation range. Finally, the prediction of the reaction zone thickness is further off compared to the prediction based on the flame speed calibration. To summarize these calibration results, using flame thickness observations provides a reduced model that can efficiently predict this flame's feature at the expanse of other features non considered in the procedure.
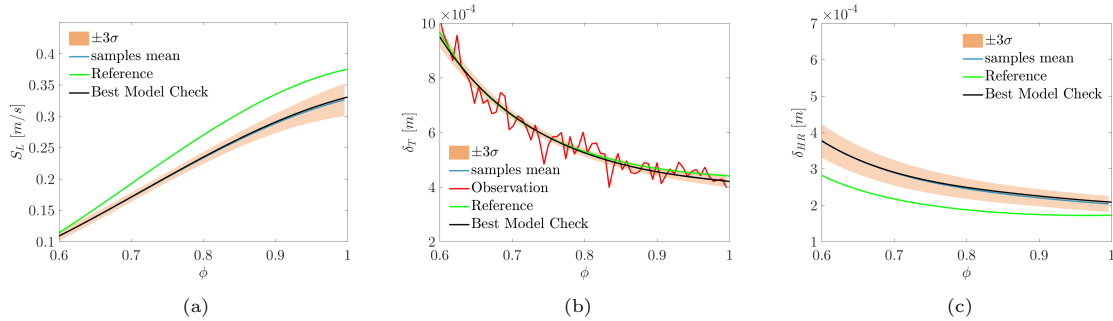

Figure 9: A posteriori predictions of (a) flame speed, (b) thermal flame thickness and (c) reaction zone thickness compared with the detailed kinetic mechanism (Reference). Case of the flame thickness calibration.

3.3. Calibration based on both flame speed and thermal flame thickness

The third calibration intends to predict correctly S_L and δ_T simultaneously. To this end, the likelihood function is the product of Eqs. 13 and 14 as follows

$$\mathcal{L}\left(\boldsymbol{S}_{\mathrm{L}}{}^{obs}, \boldsymbol{\delta}_{\mathrm{T}}{}^{obs} \,\middle|\, \boldsymbol{\xi}, \sigma_{\epsilon,S_L}^2, \sigma_{\epsilon,\delta_T}^2 \right) = \mathcal{L}_{S_L}\left(\boldsymbol{S}_{\mathrm{L}}{}^{obs} \,\middle|\, \boldsymbol{\xi}, \sigma_{\epsilon,S_L}^2 \right) \mathcal{L}_{\delta_T}\left(\boldsymbol{\delta}_{\mathrm{T}}{}^{obs} \,\middle|\, \boldsymbol{\xi}, \sigma_{\epsilon,\delta_T}^2 \right) \tag{15}$$

Figure 10 depicts the posteriors marginals of the global model parameters estimated by MCMC sampling. From the plots in the diagonal part of the figure, one can appreciate significant changes between the prior and the posterior marginal distributions of the parameters compared to the previous experiments. This evolution reflects the impact of incorporating more information (observations) in the calibration, which results in

11

better definitions of the plausible parameter's value and tighter posterior. However, while some parameters' posterior variability reduces drastically, other parameters remain quite uncertain after calibration. As expected, all the essential parameters identified in the a priori sensitivity analysis undergo a noticeable variance reduction through the calibration. More surprisingly, other parameters with a priori unimportant effects on the flame speed and thickness, such as n_{CH_4}, experience a considerable change between their marginal posterior and prior. This behavior illustrates that parameters with relatively weak influence on individual flame features can still be learned when the calibration combines various features.

The plots below the diagonal of Fig. 10 show the joint posterior marginals of all pairs of model parameters. A strong positive correlation between $E_{a,1}$ and β_1 stands out among all other correlations. However, other more subtle positively correlated parameters such as $n_{O_2,1} - \beta_1$, $n_{O_2,1} - n_{CH_4}$, $E_{a,1} - n_{O_2,1}$, and the negatively correlated $E_{a,1} - n_{CH_4}$ pair are also identified. Such detailed information on the joint-PDF of parameters is essential to hereinafter propagate the posterior uncertainties of the global chemical mechanism.

Table 5 reports the MAP value of the parameters estimated from the Markov Chain. These values differ significantly from the nominal values presented in Table 2 and are also different from the MAP values obtained when calibrating the model using either flame thickness or flame speed.

Table 5: MAP values of the model parameters calibrated using both S_L and δ_T observations. Parameters in the first row are in SI units except for the activation energies ($E_{a,i}$) in cal/mol. Pre-exponential factors (A_i) are reported in cgs units in the second row.

A_1	β_1	n_{CH_4}	$n_{O_2,1}$	$E_{a,1}$	A_2	β_2	$n_{O_2,2}$	n_{CO}	$E_{a,2}$
1.9730×10^9	0.1085	1.4892	1.1849	3.4357×10^4	1.9809×10^6	0.0090	0.5427	0.9198	1.1406×10^4
2.1864×10^{15} in cgs					1.1799×10^9 in cgs				

As for the previous calibration experiment, we present in Fig. 11 the mean values and $\pm 3\sigma$ confidence intervals of the flame speed, thermal flame thickness, and reaction zone thickness. We recall that these quantities are based on MCMC samples of the model parameters posterior and the surrogate models constructed in § 2.2. The plots also show the flame characteristics computed with the reference model (detailed chemistry) and the noisy observations used for the calibration. Again, we consider in this experiment a centered Gaussian noise with standard deviation σ_ϵ set to 10% of the reference flame feature value at $\phi = 0.8$.

We see that using flame's speed and thickness observations results in predictions of S_L and δ_T with low posterior variance and a satisfactory agreement with their reference counterparts. However, a closer comparison reveals that the $\pm 3\sigma$ confidence intervals of the predictions do not consistently contain the reference values of all ϕ. Instead, the calibration produces a trade-off between the two types of predictions. This behavior underlines the limitation of using constant parameters in the two-step global model, even for one-dimensional premixed flames in lean conditions. We also remark that the surrogates are not responsible for the absence of a complete agreement with the references since the surrogates' means of S_L and δ_T agree well with the evaluations of the global model using the inferred MAP values (Best Model Check). In contrast with the predictions of the flame's speed and thickness, the model vastly overestimates the reaction zone thickness δ_{HR} with higher discrepancies than the previous calibrations experiments. We again explain the deterioration of these predictions by the global model's limitation, which is not rich enough to predict all the laminar flame dynamics' complexity. Considering more information in the calibration may improve the predictions of the observed quantities. Still, it can be detrimental to the robustness of the model and, in particular, its ability to adequately predict other features of interest. Yet, this limitation of the global model is not necessarily critical unless one is specifically interested in predicting quantities not involved in the calibration. On the contrary, for aerothermal simulations, the flame's dynamics are mainly governed by the flame speed and thickness. A limited global model, predicting these features correctly, can produce meaningful predictions at a low computational cost.

To complete the discussion on the calibration, we repeat the previous exercise but for observations of the flame's S_L and δ_T corrupted with a lower noise level σ_ϵ. We set a σ_ϵ corresponding to 5% of the respective flame's features at $\phi = 0.8$, instead of the 10% used previously. Decreasing the noise in the observations makes more significant the contribution of the reduced model error: as σ_ϵ goes to zero, the discrepancy with the observations reduces to the error incurring to the reduction of the detailed model. In such a situation,
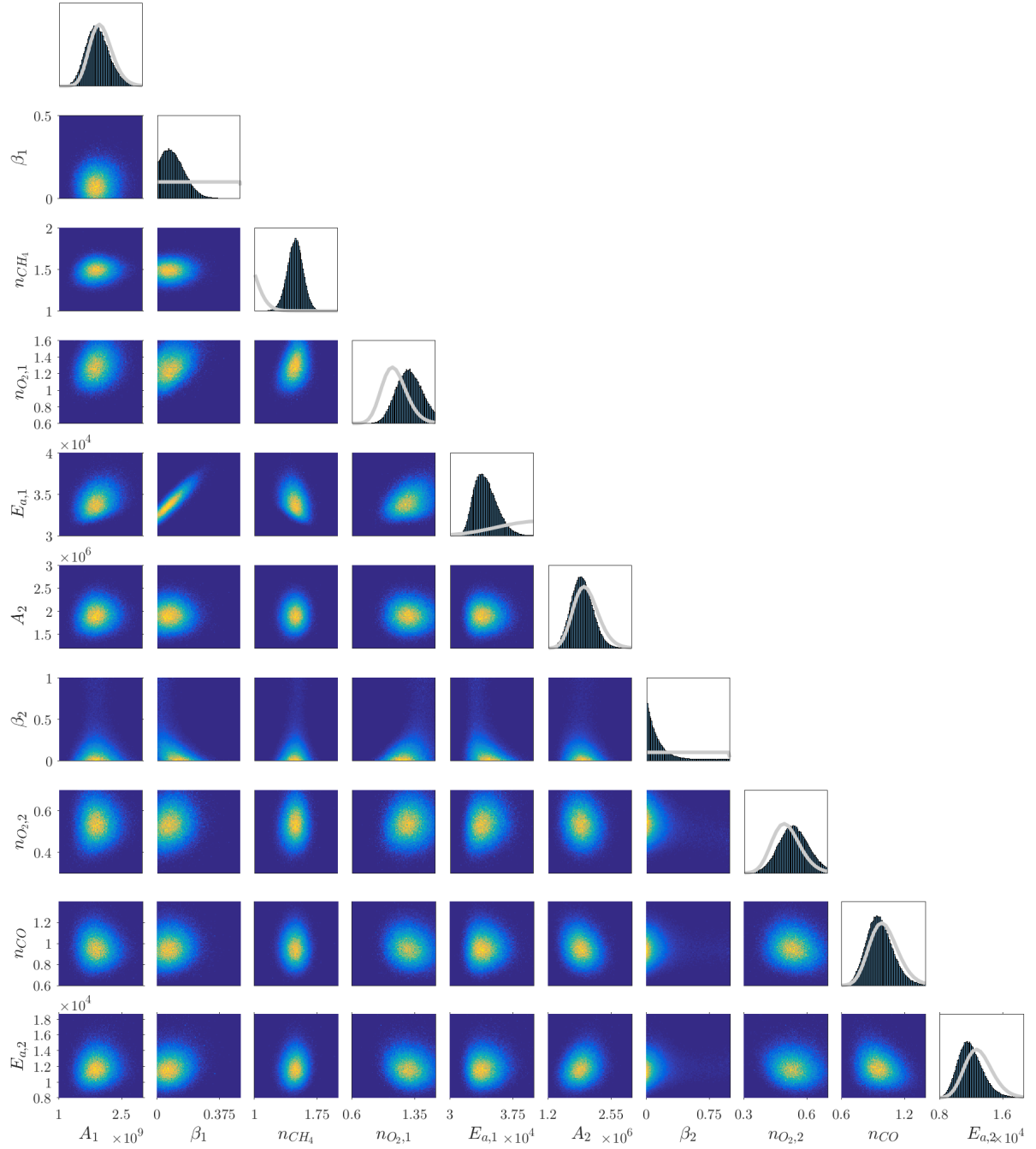
Figure 10: One-dimensional and two-dimensional posterior marginals of the model parameters for the calibration based on both the flame speed and the thermal flame thickness. In the 1-D marginal distributions reported in the diagonal, the gray lines correspond to parameters' prior.

the calibration must account for the model error when learning the parameters [49, 50].

However, the approach does not include a treatment of model error. Because the reduced model is not able to produce predictions with arbitrary low discrepancy level, consistent with the observation noise, the posterior of the parameters concentrates around the maximum of the likelihood as σ_ϵ decreases. This
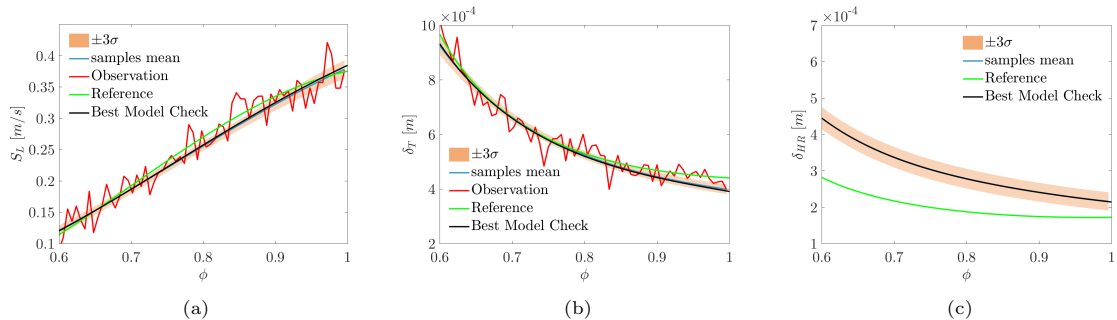
Figure 11: A posteriori results of (a) flame speed, (b) thermal flame thickness and (c) reaction zone thickness compared with the detailed kinetic mechanism (Reference) when calibration is based on both the flame speed and the thermal flame thickness.

concentration has two unfortunate consequences that we want to illustrate here. First, the tight posterior can lead to false certainty regarding the parameters' value and over confidence in the subsequent model predictions, especially for quantities not involved in the calibration procedure. Second, it is frequent that the "best" agreement between the reduced model and the observations corresponds to extreme parameter values, because lowering σ_ϵ amounts to decrease the prior's contribution to the posterior. In our method, which relies on a surrogate model to predict the features, this effect is extremely detrimental.

Figure 12, to be compared with Fig. 11, illustrates the concentration of the posterior for the surrogate's flame speed and thickness: the two features present a lower variability with a better agreement between the mean predictions and the reference solution (detailed model). Yet, the prediction of δ_{HR} is degrading for all the considered ϕ range. Further, the Figure reports the evaluations of the reduced model at the MAP of the posterior (best model check). In contrast of the previous examples (with a σ_ϵ of 10%), the best model check is found far off the surrogate posterior mean and even not inside the posterior uncertainty range. This illustrates that the calibration yields extreme parameters values for which the feature surrogates are not accurate enough. The analysis of the normal canonical variables of the MAP reveals that 3 out of 8 are found outside their initial 99.97% initial individual confidence interval, and 6 outside their prior 99.5% confidence interval. The most extreme canonical variable is found at 3.9 standard deviations from its nominal value. For comparison, in the case of the MAP with 10% σ_ϵ, only 1 canonical variable is outside its 3 standard deviation prior confidence interval; the second largest is at 1.43 standard deviation from its nominal value and all the others in less than 1 standard deviation. In terms of densities, the ratio of the prior for the two MAP points is $\sim \exp(51)$ (about 10^{22}). Concretely, building accurate surrogates over such low probability region of the prior would be too demanding without relying on an adaptive method (see for instance [51]). Trying to improve the surrogates accuracy is not pursued here because, fundamentally, the calibration with low observation noise would demand an appropriate treatment of the model error. Instead, we proceed with the exploitation of the reduced model calibrated with the 10% observation noise, for which the model error does not compromise the inference.
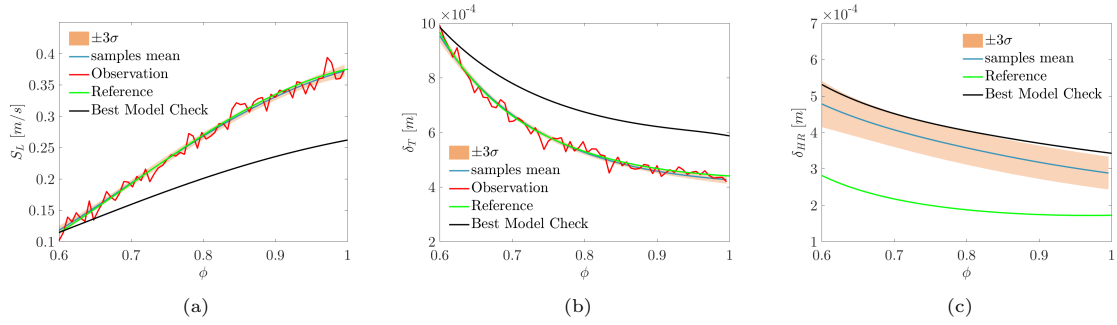
Figure 12: A posteriori results of (a) flame speed, (b) thermal flame thickness and (c) reaction zone thickness compared with the detailed kinetic mechanism (Reference) when the calibration is based on both the speed and the thickness of the flame, but considering a low value of σ_ϵ.

4. Application to flame-vortex simulation

We now assess the predictive capabilities of the inferred reduced model when applied on a situation differing significantly from the conditions considered for its calibration. Specifically, we consider a two-dimensional flame-vortex interaction in unsteady laminar regime, corresponding to a configuration widely studied numerically [52–54] and experimentally [55–57]. Because this configuration includes the phenomenology of stretched flames, it has been used to validate numerical methods and models in reactive flows [58, 59]. A detailed review on flame-vortex interactions can be found in [60].

4.1. Numerical test case description

The problem, sketched in Fig. 13, consists of an initially planar flame front interacting with a convected pair of counter-rotating vortices.
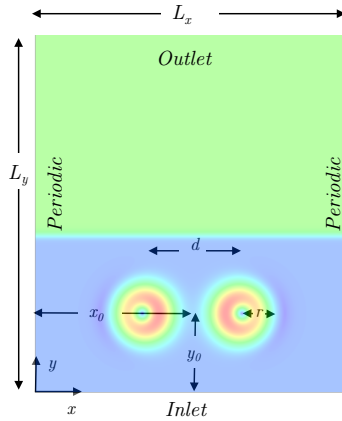

Figure 13: Schematic of the initial configuration for the two-dimensional flame-vortex interaction. The vortices are colored by velocity magnitude.

15

The initial condition is a stationary one-dimensional flame profile superposed with a pair of counter-rotating vortices; the velocity field is given by

$$u_1(x,y) = (y - y_0)\left(\kappa_r(x,y) + \kappa_l(x,y)\right), \tag{16}$$

and

$$u_2(x,y) = u_{2,0} - (x - x_0 - \frac{d}{2})\kappa_r(x,y) - (x - x_0 + \frac{d}{2})\kappa_l(x,y), \tag{17}$$

where u_1 and u_2 are the horizontal and vertical velocity components; $u_{2,0}$ is the velocity of the stationary one-dimensional flame; (x_0, y_0) is the center of the vortex pair (see Fig. 13); d is the distance between the vortex centers; $\kappa_l(x,y)$ and $\kappa_r(x,y)$ are the vortex intensity fields associated to the left and right vortices, respectively. In the following, we consider a symmetric configuration with $d = 6.25 \times 10^{-3}$ m and

$$\kappa_{r,l}(x,y) = \pm\frac{\tau}{r^2} \exp\left(-\frac{(x - x_0 \mp \frac{d}{2})^2 + (y - y_0)^2}{2r^2}\right), \tag{18}$$

where the vortices core size is set to $r = 10^{-3}$ m and the vortex intensity to $\tau = 6.5 \times 10^{-3} \mathrm{m}^2\mathrm{s}^{-1}$. These values, similar to the case in [54], lead to a combustion regime with thickened wrinkled flames and formation of gas pockets [52].

As indicated in Fig. 13, the top boundary of the domain is an outlet, while the bottom is the inlet where we apply the solution of the one-dimensional flame with a constant speed ($u_2 = S_L = 0.2877$ m/s), equivalent ratio $\phi = 0.83$, temperature (300 K) and pressure (1 atm). Finally, the periodic conditions apply to the left and right boundaries. The domain size is set to $L_x = 2 \times 10^{-2}$ m and $L_y = 3 \times 10^{-2}$ m in order to minimize the impact of computational boundaries on the interaction. The low Mach-number Navier-Stokes equations and the species transport equations are solved using the YALES2 solver [61] on a uniform Cartesian mesh of 600×900 nodes and a constant grid spacing $\triangle x = \triangle y = 3.33 \times 10^{-5}$ m. The YALES2 solver is an optimized parallel finite volume method code. We used the low-storage Runge-Kutta scheme with four steps to integrate the governing equations in time and a central 4th-order scheme for spatial discretization. For stability, we set the maximal Courant-Friedrichs-Lewy (CFL) number to CFL=0.3, and the Fourier number (Fo) to Fo=0.1.

4.2. Reference solution of flame-vortex interactions

A reference simulation of the flame-vortex computation is first computed using the detailed mechanism GRI 3.0 [31]. Figure 14 shows the time evolution of the integrated heat release rate (I_{HR}) over the computational domain,

$$I_{HR}(t) = \int_\Omega HR(t)d\Omega, \tag{19}$$

scaled by its initial value $I_{HR}(0)$. Here, we normalize the time using the reference flame speed $S_L = 0.2877$ m/s and thickness $\delta_T = 5.1046 \times 10^{-4}$ m. The evolution presents different periods characteristic of the flame-vortex interaction dynamics. After an initial phase where I_{HR} remains nearly constant ($t^* \lesssim 4.5$), the flame gradually stretches as the vortex pair approaches and distort the flame front, creating wrinkles. The elongation of the flame front improves the mass burning rate inducing a continuous increase of I_{HR}. The first row of Fig. 15 depicts the flow structure at $t_1^* = 6.54$ when I_{HR} is increasing; in this phase, the flame is attached to the vortex and rolls up. Eventually, I_{HR} peaks at $t^* \approx 7.6$ before initiating a fast decaying phase. The peak of I_{HR} coincides with the closing of a neck of fresh gases connecting the vortex region with the primary flame front; see the second row of Fig. 15 corresponding to $t_2^* = 7.67$. The closing of the neck forms pockets of fresh gases that burn rapidly, causing a sharp decrease of I_{HR}, as illustrated in the third row of Fig. 15 for $t_3^* = 8.45$. These different stages of the vortex-flame interaction are consistent with previous studies [52, 54, 58].
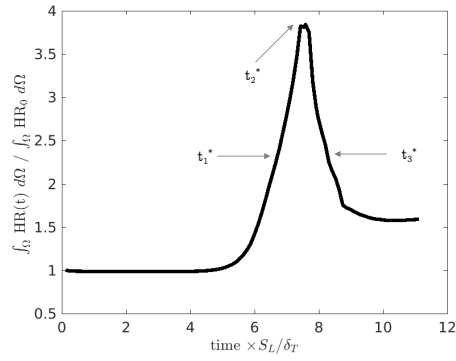
Figure 14: Time evolutions of I_{HR} normalized by its initial value for the reference solution using the detailed chemical scheme GRI 3.0 [31].
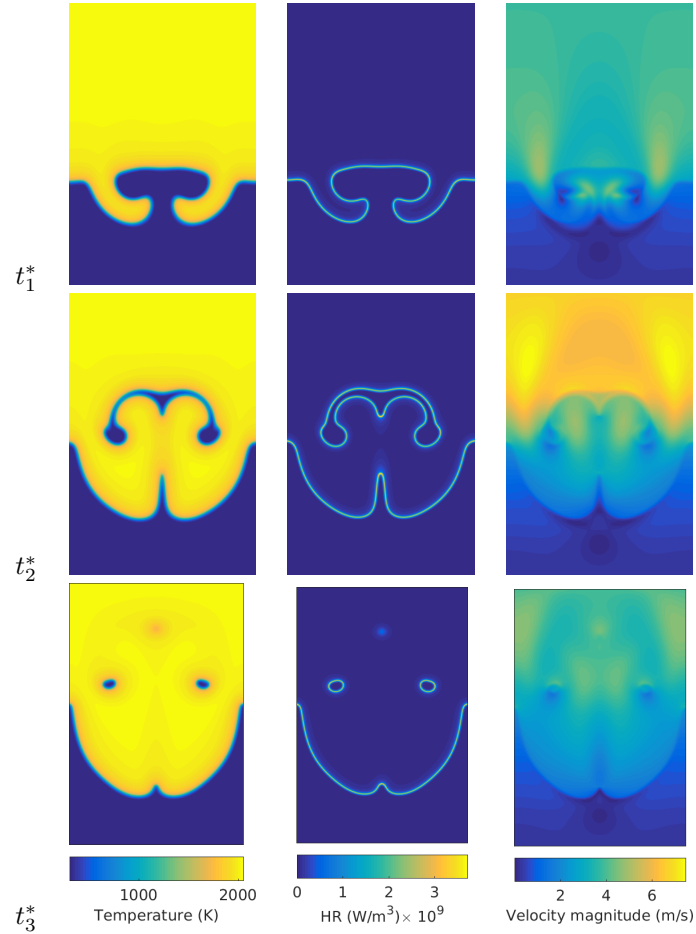

Figure 15: Reference temperature, heat release rate (HR), and velocity magnitude fields of the 2D flame-vortex DNS using GRI 3.0 [31] detailed chemistry. The fields are shown at normalized times t^* corresponding to the different phases of the flame-vortex interaction and indicated in Fig. 14.

17

4.3. Flame-vortex prediction for the calibrated two-step global model

Samples of the reduced two-step mechanism, drawn from the posterior distribution corresponding to the calibration on S_L and δ_T data, are used to simulate the flame-vortex problem. A total of 60 independent samples are drawn from the model's posterior distribution using the Markov chain. These model samples are exploited to assess the effects of calibration uncertainty in a much more complex configuration than the calibration experiment (one-dimensional laminar flame).

We start by presenting in Fig. 16 the spread of the predictions for the 60 models reporting the isoline $c = 0.5$ of the progress variable based on temperature. The isolines are shown at the three times t_1^*, t_2^* and t_3^*, previously discussed. Note that in all cases, the normalization of the times uses the reference flame speed and thickness ($S_L = 0.2877$ m/s and $\delta_T = 5.1046 \times 10^{-4}$ m). The figure also reports the isolines $c = 0.5$ of the best candidate model (MAP) and the reference solution (detailed chemistry). It is observed that the spread of the isolines $c = 0.5$ is increasing between t_1^* and t_2^*. The posterior uncertainty is particularly large in intense roll-up areas during the first phase (see t_1^*) and at the boundary of the entrapped fresh-gases pockets at peak time (see t_2^*). The highest variability in these areas is not surprising as rolling-up and entrapment processes involve curvature effects that were not present in the one-dimensional flame experiment considered for the calibration. However, the prediction uncertainty reduces as the decaying phase advances (see t_3^*). In particular, the location of the isolines of $c = 0.5$ from the inlet's fresh gases is not much uncertain. Finally, the differences between the reference (black) and MAP (red) model predictions are reasonably small at all the times shown, while the reference isoline is always within the sample set's isolines.
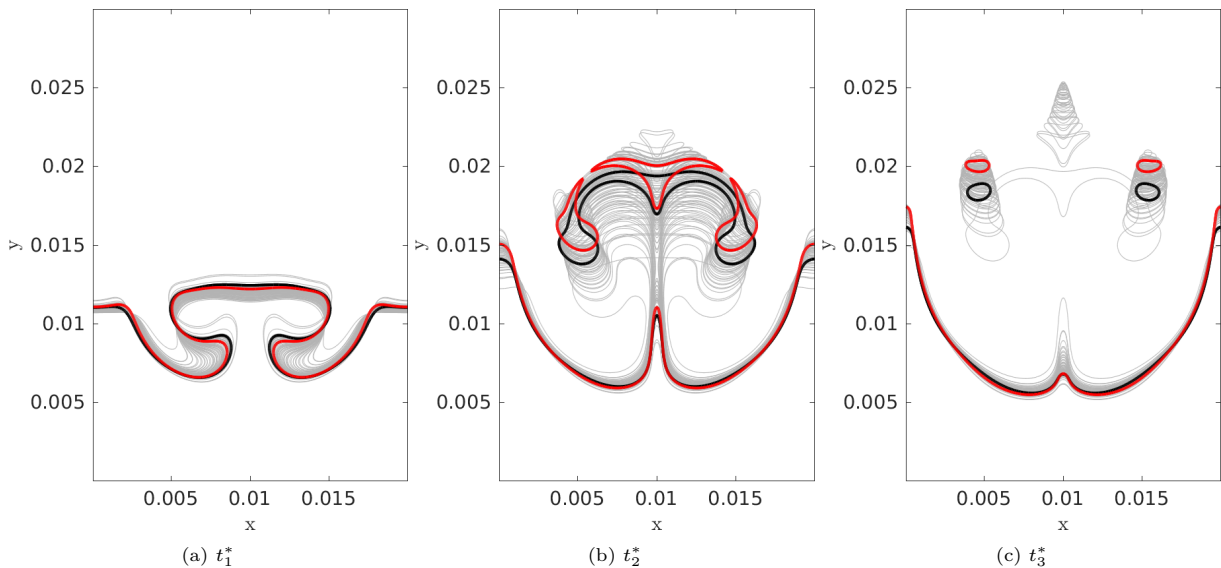

(a) t_1^* (b) t_2^* (c) t_3^*

Figure 16: Progress variable isolines $c = 0.5$ at (a) t_1^*, (b) t_2^* and (c) t_3^*. Thin gray lines correspond to the samples of the reduced models, the black line refers to the detailed chemistry model, while the red line corresponds to MAP model.

We now focus on global flame behavior to better assess the calibrated model's predictive capabilities in the flame-vortex interaction. Figure 17 shows the time-evolutions of the normalized I_{HR}, and flame surface S_f define by

$$S_f = \int_\Omega |\nabla c(t)| d\Omega. \tag{20}$$

The plots report the solutions computed with the 60 samples of the calibrated model, together with the average of the samples (blue lines) and ± 3 standard deviation confidence interval (shaded areas), MAP model prediction (red lines), and reference solution (black lines). As for the isolines of $c = 0.5$ presented above, the reference solutions fall within the confidence intervals, and the agreement between the posterior mean predictions, MAP model predictions, and reference solutions are reasonably good. The samples indicate

18

that the calibrated two-step model tends to overestimate I_{HR} and flame surface's peak values. The posterior uncertainty in the two-step model parameters mostly translates into uncertainty in the presented quantities' growth and decay rates. The uncertainty impact explains that the posterior mean predictions are in better agreement with the reference than the MAP prediction. The samples' spread is mostly explained by the variability of their respective laminar flame speed, which induces time-shifts in the I_{HR} and flame surface evolutions. Indeed the inlet velocity is set to the reference laminar flame velocity S_L for all samples, leading to differences in relative convective velocity between the vortex pair and flame front, depending on the particular model sampled. We further illustrate the fundamental role of the flame thickness and the laminar flame speed in the dynamics of the vortex-flame interactions in Fig. 18. The figure shows the evolutions of the normalized flame surface for the different samples as functions of the time normalized by the respective values of speed S_L^* and thickness δ_T^* associated with each sample of the model. With this sample-dependent time-scaling, the spread of the curves dramatically reduces, demonstrating that, for this global quantity, the impact of the calibrated two-step model uncertainty mostly translates into a time-scale uncertainty.
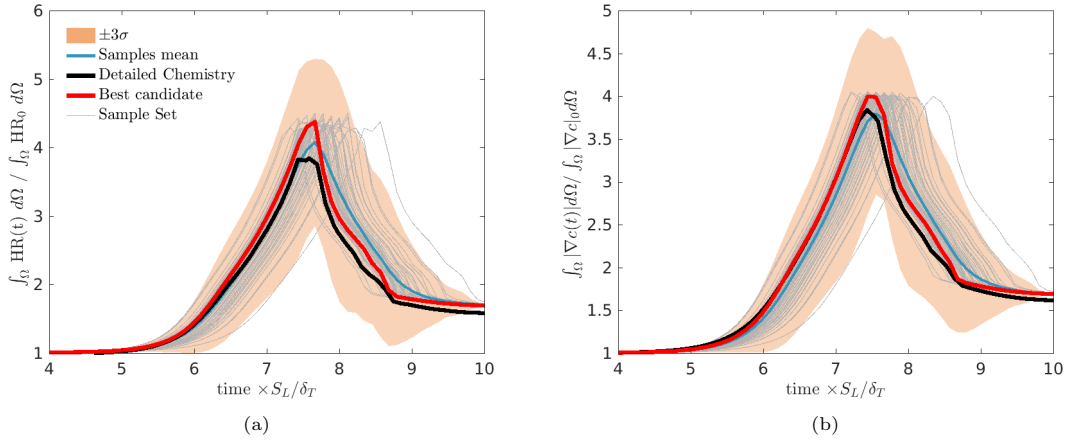

Figure 17: Time evolutions of the (a) normalized I_{HR} and (b) flame surface, for the calibrated two-step model. The time is normalized using the reference flame speed and thickness. The MAP and reference (using GRI 3.0 [31]) predictions are also reported.
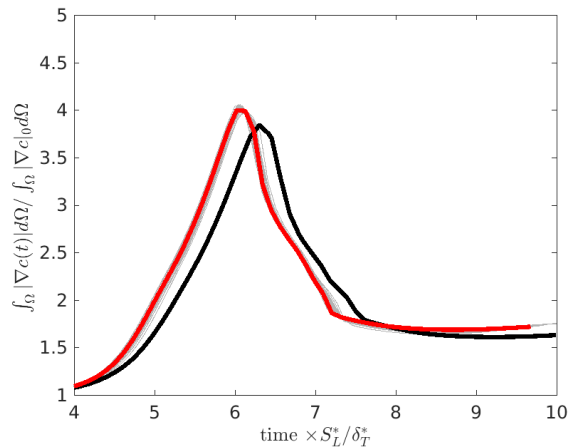

Figure 18: Time evolutions of the normalized flame surface versus dimensionless time for the calibrated two-step model. Contrary to the plot in Fig. 17, the normalization of time uses the flame speed and thickness of each sample. The MAP and reference (using GRI 3.0 [31]) predictions are also reported.

19

To complete the analysis of the predictive capability of the calibrated two-step model, we consider a more challenging integral quantity which is much sensitive to flow stretching. Specifically, we focus on the dependence of I_{HR} on the flame surface S_f and report in Fig. 19 the evolutions of their normalized ratio ψ, defined as

$$\psi(t) = \frac{\int_\Omega HR(t)d\Omega}{\int_\Omega |\nabla c(t)|d\Omega} \left(\frac{\int_\Omega HR_0 d\Omega}{\int_\Omega |\nabla c_0|d\Omega} \right)^{-1}. \tag{21}$$

This choice is motivated by the tangential velocity gradients' critical role in the reaction zone (the "flame surface"). The tangential gradient modifies the local burning rate, affecting the chemical composition and the whole dynamics of the premixed flame, in particular for mixtures with non-unit Lewis numbers. The prediction of these highly non-linear processes, summarized here in the time evolutions of $\psi(t)$, is challenging for models that have not been calibrated on flames presenting such complicated features. This difficulty is illustrated in Fig. 19. Although the reference and reduced model predictions present somehow similar evolution in time, a significant increase in the samples variability of $\psi(t)$ is reported after the peak time of I_{HR} and S_f ($t^* > 7$), that is when stretching is maximum with the formation of fresh gas pockets. Again, the spread could be reduced, to some extend, by relying on a time-scaling of the individual samples. However, contrary to the previous quantities I_{HR} and S_f, the reference solution is not contained in the ± 3 standard deviations bounds of the reduced model prediction. This mismatch denotes the inadequacy of the model and the predictive limitations of the two-step model calibrated on un-stretched laminar flames.
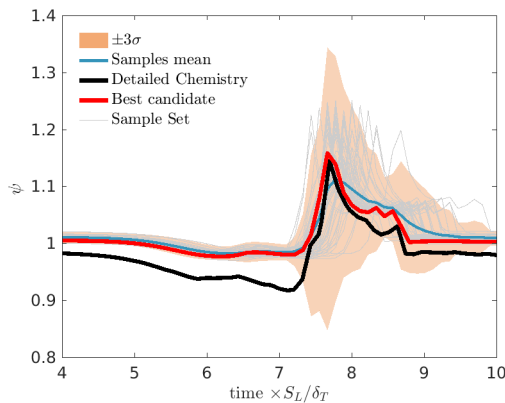

Figure 19: Time evolutions of $\psi(t)$ (see Eq. 21) for the calibrated two-step model. The MAP and reference (using GRI 3.0 [31]) predictions are also reported.

5. Conclusions

This work concerns the Bayesian inference of a reduced two-step reaction mechanism for CH_4, using observations of one-dimensional premixed laminar flames' main physical features. Specifically, the calibration of the global chemistry model parameters employs synthetic observations of the laminar flame speed or/and thickness, generated from simulations using the GRI 3.0 methane detailed chemical mechanism.

To alleviate most of the Bayesian inference's computational burden, we first construct surrogate models of the reduced model flames' characteristics. These surrogates combine a PCA to account for the dependence on the equivalent ratio and PC expansions for the dependencies in the model parameters. The normalized mean squared error of the surrogates, estimated on additional validation sets, are 1.44% for the thermal flame thickness, 1.94% for the reaction zone thickness, and 1.97% for the laminar flame speed.

We conduct three different inference exercises using: (i) flame speed observations, (ii) thermal thickness observations, and (iii) both flame speed and thermal thickness observations. The surrogate models of the flame's characteristics allow running the Metropolis-Hasting algorithm to draw 10^7 samples from the

parameters' approximated joint posterior. In all three calibration exercises, the differences between the prior and posterior marginals are significant for only a subset of parameters, while the information gain on other parameters is negligible. An a priori sensitivity analysis can anticipate the set of parameters informed by the observations. The posteriors' marginals of the informed parameters are also sensitive to the observations used for the calibration. While these marginals are similar when using laminar flame speed or thermal thickness observations, they can differ significantly when the two types of observations are combined. We show that these differences translate in improved predictions of the flame's speed and thickness, with lower a posteriori spreads. However, these improvements come with the degradation of other flame characteristics not involved in the calibration, such as the thermal flame thickness. This behavior reflects the global model's insufficiency, which is not complex enough to predict all the laminar flames' features.

To further appreciate the calibrated model's predictive capability and its posterior uncertainty, we finally consider its application to the simulation of a two-dimensional DNS flame-vortex configuration. We assess the quality of the posterior predictions using a detailed chemistry model simulation. The comparison shows consistent predictions of the total heat release and flame surface time-evolutions, with the calibrated model's confidence intervals containing the detailed model evolutions. Additionally, the posterior predictions' variability is mostly explained by a phase variability in the flame surface evolution caused by the uncertainty in the ratio S_L/δ_T for the calibrated model.

This challenging example highlights another limitation of the 2-step model concerning the heat release rate per flame surface area. The calibrated model fails to reproduce the flame response to stretch correctly. This limitation is not surprising since the observations used to calibrate the model did not encompass stretched flame phenomenon.

As a first approach, the present work adopted constant model parameters for the 2-step global chemistry mechanisms. This approach restricts the range of fuel-air ratio to lean mixtures. We plan to extend the Bayesian inference to model parameters functions of the equivalence ratio in the future. Future calibration should also incorporate other flame phenomena to provide models capable of handling more complex situations. The growing need for accurate and error-bounded results in modern combustion simulations turns this well-grounded methodology into a promising approach to derive the new generation of stochastic global chemical schemes accounting for posterior uncertainty.

Acknowledgments

Appendix A. Model reduction

The original data correspond to $N_s = 10^4$ samples of the global feature considered (S_L, δ_T and δ_{HR}) evaluated at $N_\phi = 51$ values of the equivalent ratio covering the range $0.6 \leq \phi < 1$. Denoting S_L, δ_T or δ_{HR} by v; we then write $\boldsymbol{v}^i = (v_1^i \cdots v_{N_\phi}^i)^\top$, for $i = 1, \ldots, N_s$, the feature vector of the samples. Let $[V]$ be the matrix gathering the $\boldsymbol{v}^i$:

$$[V] = [\boldsymbol{v}^1 \cdots \boldsymbol{v}^{N_s}] \in \mathbb{R}^{N_\phi \times N_s}. \tag{A.1}$$

To ensure positivity of the final reduced model, we apply the PCA on the data preconditioned by applying the logarithmic transformation to $[V]$. In other words, we seek for the reduced modes of $[\ln V]$ where, in the present context, the logarithm is understood to apply entry-wise to matrices and vectors; for instance, $([\ln V])_{i,j} = \ln([V]_{i,j})$. We denote $[C] \in \mathbb{R}^{N_\phi \times N_\phi}$ the SSCP (sum-of-squares-and-cross-products) matrix associated to $[\ln V]^\top$,

$$[C] \doteq [\ln V][\ln V]^\top. \tag{A.2}$$

Clearly, $[C]$ is symmetric and non negative. Let $(\lambda_k, \boldsymbol{l}_k)_{1 \leq k \leq N_\phi}$ be the normalized eigen-pairs of $[C]$ satisfying

$$[C]\boldsymbol{l}_k = \lambda_k \boldsymbol{l}_k, \quad \boldsymbol{l}_k^\top \boldsymbol{l}_{k'} = \delta_{k,k'}. \tag{A.3}$$

The eigenvalues being real and non-negative, they can be sorted by decreasing value, $\lambda_1 \geq \cdots \geq \lambda_{N_\phi} \geq 0$, and we can set N_{red} the smallest positive integer such that

$$\sum_{k=1}^{k=N_{red}} \lambda_k \geq (1-\epsilon) \sum_{k=1}^{k=N_\phi} \lambda_k, \tag{A.4}$$

for some positive $\epsilon \ll 1$. In the present work we used $\epsilon = 10^{-6}$, leading a negligible reduction error, and an adequate reduced representation of the original feature vectors $\boldsymbol{v}^i$. The reduced basis is expressed as

$$[L] = [\boldsymbol{l}_1 \cdots \boldsymbol{l}_{N_{red}}] \in \mathbb{R}^{N_\phi \times N_{red}}. \tag{A.5}$$

The vector $\boldsymbol{a}^i$ of the reduced coordinates associated to the i-th sample of the feature vector is obtained by projecting $\ln \boldsymbol{v}^i$ onto the reduced basis $[L]$:

$$\boldsymbol{a}^i \doteq [L]^\top \ln \boldsymbol{v}^i.$$

The previous expression readily extends to the case of the random feature vector $\boldsymbol{v}(\boldsymbol{\xi})$ to obtain the random reduced coordinated $\boldsymbol{a}(\boldsymbol{\xi}) = [L]^\top \ln \boldsymbol{v}(\boldsymbol{\xi})$, leading to the reduced approximation

$$\boldsymbol{v}(\boldsymbol{\xi}) \approx \exp\left[[L]\boldsymbol{a}(\boldsymbol{\xi})\right]. \tag{A.6}$$

The reduced modes of the ensemble of samples are shown in Fig. A.20 for the 3 features considered in this work. Three to four reduced modes are needed to satisfy the error criterion in (A.4).
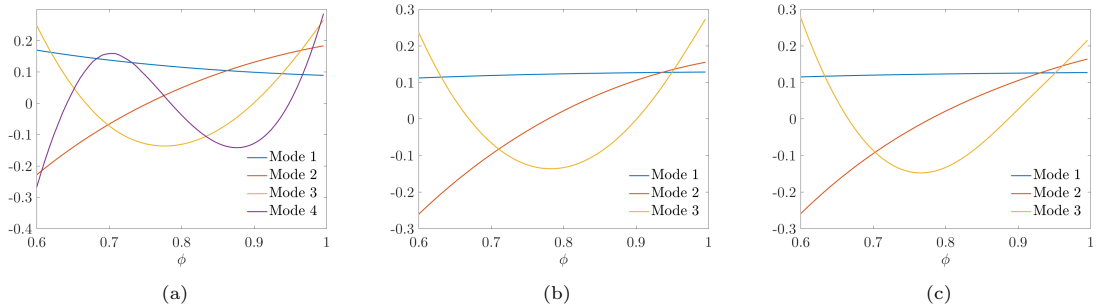

Figure A.20: Dominant reduced modes for the flame velocity (a), thermal flame thickness (b), and reaction zone thickness (c). The reduction uses $N_s = 10^4$ samples of the feature vectors corresponding to a QMC sample set of the prior global model.

Appendix B. Polynomial chaos expansion

To construct the surrogates of the global features, it remains to approximate the dependences on $\boldsymbol{\xi}$ of the reduced coordinates $\boldsymbol{a}(\boldsymbol{\xi})$. To this end we introduce a PC basis of orthonornal random polynomials $\Psi_\alpha(\boldsymbol{\xi})$. The PC polynomials are orthonormal in the sense that

$$\mathbb{E}\left[\Psi_\alpha \Psi_{\alpha'}\right] \doteq \int \Psi_\alpha(\boldsymbol{\xi})\Psi_{\alpha'}(\boldsymbol{\xi})p(\boldsymbol{\xi})d\boldsymbol{\xi} = \delta_{\alpha,\alpha'},$$

where $p(\boldsymbol{\xi})$ is the probability density function of the canonical random variables. The latter being independent standard Gaussian or uniformly distributed random variables, the random polynomials Ψ_α are the

product of univariate Hermite (Gaussian) and Legendre (uniform) polynomials. With these notations, and assuming the reduced coordinates $\boldsymbol{a}(\boldsymbol{\xi})$ are second order random variables, they can be expanded as

$$\boldsymbol{a}(\boldsymbol{\xi}) = \sum_{\alpha=1}^{\alpha=\infty} \boldsymbol{a}_\alpha \Psi(\boldsymbol{\xi}).$$

In practice, the PC expansion of $\boldsymbol{a}$ must be truncated. In this work, we classically use the total degree truncation, fixing an expansion order N_o. The truncation results in the truncated approximation,

$$\boldsymbol{a}(\boldsymbol{\xi}) \approx \sum_{\alpha=1}^{\alpha=N_{pol}} \boldsymbol{a}_\alpha \Psi(\boldsymbol{\xi}), \tag{B.1}$$

with PC coefficients $\boldsymbol{a}_\alpha$ to be estimated. Several approach are available for the estimation of the PC coefficients; in the present work we found suitable to apply a classical least squares minimization problem derived as follows. The projection error, expressed as

$$\Delta^2(\boldsymbol{a}_1, \cdots, \boldsymbol{a}_{N_{pol}}) \doteq \mathbb{E}\left[\left\| \boldsymbol{a}(\boldsymbol{\xi}) - \sum_{\alpha=1}^{\alpha=N_{pol}} \boldsymbol{a}_\alpha \Psi(\boldsymbol{\xi}) \right\|^2 \right], \tag{B.2}$$

is substituted with the samples average:

$$\widetilde{\Delta}^2(\boldsymbol{a}_1, \cdots, \boldsymbol{a}_{N_{pol}}) \doteq \sum_{i=1}^{i=N_s} \left\| \boldsymbol{a}(\boldsymbol{\xi}^i) - \sum_{\alpha=1}^{\alpha=N_{pol}} \boldsymbol{a}_\alpha \Psi(\boldsymbol{\xi}^i) \right\|^2. \tag{B.3}$$

The minimization of this sum of squared residual is straightforward, recognizing that the determination of the minimization over the different reduced coordinates separates. Therefore, the minimization requires the inversion of a single $N_{pol} \times N_{pol}$ symmetric matrix $[Z]^\top[Z]$, where $[Z]$ is the matrix of regressors (PC basis polynomials evaluated at the sample points)

$$[Z]_{i,\alpha} \doteq \Psi_\alpha(\boldsymbol{\xi}^i).$$

For $1 \leq l \leq N_{red}$, the minimization problem for the PC coefficients of $a_l(\boldsymbol{\xi})$ writes

$$[Z]^\top[Z](a_{l,1} \cdots a_{l,N_{pol}})^\top = [Z]^\top(a_l^1 \cdots a_l^{N_s})^\top.$$

We also remark that the matrix Z is the same for all the global features, since they rely on the same sample points.

Once the PC coefficients $\boldsymbol{a}_\alpha = (a_{1,\alpha} \cdots a_{N_{red},\alpha})^\top$ of the reduced coordinates are determined, the surrogate of the feature vector is finally given by

$$\boldsymbol{v}(\boldsymbol{\xi}) \approx \boldsymbol{v}_{PC}(\boldsymbol{\xi}) \doteq \exp\left([L] \sum_{\alpha=1}^{\alpha=N_{pol}} \boldsymbol{a}_\alpha \Psi_\alpha(\boldsymbol{\xi}) \right), \tag{B.4}$$

where the exponential operator is understood to apply componentwise to vectors.

Appendix C. Markov chain Monte-Carlo (MCMC)

Let $\boldsymbol{v} \in \mathbb{R}^{N_\phi}$ be the true feature vector and $\boldsymbol{v}^{obs}$ its observation. We assume that the observation error $\boldsymbol{\epsilon}^{obs} = \boldsymbol{v} - \boldsymbol{v}^{obs}$ is a centred Gaussian vector with covariance matrix Σ_ϵ^2. Following this assumption, the

likelihood of the observations ϵ^{obs} for a given value of the canonical variables $\boldsymbol{\xi}$ is a multivariate normal distribution:

$$\mathcal{L}\left(\boldsymbol{v}^{obs}|\boldsymbol{\xi}\right) = \frac{1}{\sqrt{(2\pi)^{N_\phi}|\Sigma_\epsilon^2|}} \exp\left[-\frac{1}{2}\left(\boldsymbol{v}\left(\boldsymbol{\xi}\right) - \boldsymbol{v}^{obs}\right)^T \left(\Sigma_\epsilon^2\right)^{-1}\left(\boldsymbol{v}\left(\boldsymbol{\xi}\right) - \boldsymbol{v}^{obs}\right)\right]. \tag{C.1}$$

Assuming further that the observation errors are independent and identically distributed, $\Sigma = \sigma_\epsilon^2[I]$, with $[I]$ the identity matrix, and substituting $\boldsymbol{v}(\boldsymbol{\xi})$ with its PC approximation $\boldsymbol{v}_{PC}(\boldsymbol{\xi})$ in (B.4), the likelihood function becomes

$$\mathcal{L}\left(\boldsymbol{v}^{obs}|\boldsymbol{\xi}\right) \approx \frac{1}{(2\pi\sigma_\epsilon^2)^{N_\phi/2}} \exp\left(-\frac{\left\|\left(\boldsymbol{v}_{PC}\left(\boldsymbol{\xi}\right) - \boldsymbol{v}^{obs}\right)\right\|^2}{2\sigma_\epsilon^2}\right). \tag{C.2}$$

Denoting $\pi_\xi(\boldsymbol{\xi})$ the prior density of $\boldsymbol{\xi}$, the posterior distribution $p\left(\boldsymbol{\xi}|\boldsymbol{v}_{obs}\right)$ is given by the Bayes' theorem

$$p\left(\boldsymbol{\xi}|\boldsymbol{v}^{obs}\right) = \frac{\mathcal{L}\left(\boldsymbol{v}^{obs}|\boldsymbol{\xi}\right)\pi_\xi\left(\boldsymbol{\xi}\right)}{p(\boldsymbol{v}_{obs})}, \tag{C.3}$$

where the evidence $p(\boldsymbol{v}_{obs})$ is fixed to ensure that the posterior density integrates to one. In practice, the product of the likelihood and prior of $\boldsymbol{\xi}$ can be easily evaluated relying on the PC surrogate of $\boldsymbol{v}(\boldsymbol{\xi})$. In the rest of this section, we denote $p^*(\boldsymbol{\xi}) = \mathcal{L}\left(\boldsymbol{v}^{obs}|\boldsymbol{\xi}\right)\pi_\xi\left(\boldsymbol{\xi}\right)$ and observe that $p^*(\boldsymbol{\xi})$ is equal to the posterior density up to a multiplicative constant (the evidence).

To draw samples of $\boldsymbol{\xi}$ from its posterior (C.3), we rely on the Metropolis-Hastings method. This method generates a Markov chain of successive steps $\boldsymbol{\xi}_k$ from the following algorithm:

1. Set $k = 0$ and draw at random the current state $\boldsymbol{\xi}_k$ from $p_\xi(\boldsymbol{\xi})$.
2. Draw at random $\boldsymbol{\xi}'$ from the transition density $t\left(\boldsymbol{\xi}|\boldsymbol{\xi}_k\right)$.
3. Set $r = \frac{p^*(\boldsymbol{\xi}')t(\boldsymbol{\xi}_k|\boldsymbol{\xi})}{p^*(\boldsymbol{\xi}_k)t(\boldsymbol{\xi}'|\boldsymbol{\xi}_k)}$.
4. Draw α uniformly in $(0,1)$.
5. If $\alpha < r$ set $\boldsymbol{\xi}_{k+1} = \boldsymbol{\xi}'$ otherwise $\boldsymbol{\xi}_{k+1} = \boldsymbol{\xi}_k$.
6. Increment k and repeat from step 2.

Under mild conditions concerning, in particular, the transition density $t(\boldsymbol{\xi}'|\boldsymbol{\xi})$, it can be shown that $\boldsymbol{\xi}_k \sim p(\boldsymbol{\xi}|\boldsymbol{v}_{obs})$ as $k \to \infty$. In this work, we consider reversible Gaussian transition densities such that

$$\boldsymbol{\xi}' \sim \mathcal{N}(\boldsymbol{\xi}_k, \Sigma_t^2).$$

The covariance of the transition, Σ_t^2 is crucial to generate chains with minimal correlation between successive steps (good mixing properties). To this end we relied on the classical adaptive procedure where Σ_t^2 is a scaled version of the posterior covariance, which is estimated iteratively before running the chain. Also, the steps $\boldsymbol{\xi}_k$ are considered samples of posterior only after the chain has been run long enough (i.e., k large enough) such that the starting point has no influence on the samples generated. Note that because of the reversible transition density, the ratio r in the third line of the algorithm reduces to the ratio between the densities at the proposed and current states of the chain. Therefore, the method can be applied on p^* without having to estimate the evidence.

References

References

[1] M. J. Evans, P. R. Medwell, Z. F. Tian, A. Frassoldati, A. Cuoci, A. Stagni, Ignition characteristics in spatially zero-, one-and two-dimensional laminar ethylene flames, AIAA Journal 54 (2016) 3255–3264.

[2] T. Lu, C. K. Law, Toward accommodating realistic fuel chemistry in large-scale computations, Progress in Energy and Combustion Science 35 (2009) 192–215.

[3] J. H. Chen, Petascale direct numerical simulation of turbulent combustion—fundamental insights towards predictive models, Proceedings of the Combustion Institute 33 (2011) 99–123.

[4] A. Felden, P. Pepiot, L. Esclapez, E. Riber, B. Cuenot, Including analytically reduced chemistry (ARC) in CFD applications, Acta Astronautica 158 (2019) 444–459.

[5] B. Fiorina, R. Baron, O. Gicquel, D. Thevenin, S. Carpentier, N. Darabiha, et al., Modelling non-adiabatic partially premixed flames using flame-prolongation of ildm, Combustion Theory and Modelling 7 (2003) 449–470.

[6] P. S. Volpiani, T. Schmitt, D. Veynante, Large eddy simulation of a turbulent swirling premixed flame coupling the tfles model with a dynamic wrinkling formulation, Combustion and Flame 180 (2017) 124–135.

[7] T. Steinbacher, A. Albayrak, A. Ghani, W. Polifke, Response of premixed flames to irrotational and vortical velocity fields generated by acoustic perturbations, Proceedings of the Combustion Institute 37 (2019) 5367–5375.

[8] C. Turquand d'Auzay, V. Papapostolou, S. Ahmed, N. Chakraborty, Effects of turbulence intensity and biogas composition on the localized forced ignition of turbulent mixing layers, Combustion Science and Technology 191 (2019) 868–897.

[9] T. Steinbacher, A. Albayrak, A. Ghani, W. Polifke, Consequences of flame geometry for the acoustic response of premixed flames, Combustion and Flame 199 (2019) 411–428.

[10] C. K. Westbrook, F. L. Dryer, Simplified reaction mechanisms for the oxidation of hydrocarbon fuels in flames, Combustion science and technology 27 (1981) 31–43.

[11] S. Li, F. Williams, K. Gebert, A simplified, fundamentally based method for calculating NOx emissions in lean premixed combustors, Combustion and flame 119 (1999) 367–373.

[12] A. Sánchez, A. Lépinette, M. Bollig, A. Liñán, B. Lázaro, The reduced kinetic description of lean premixed combustion, Combustion and flame 123 (2000) 436–464.

[13] L. Selle, G. Lartigue, T. Poinsot, R. Koch, K.-U. Schildmacher, W. Krebs, B. Prade, P. Kaufmann, D. Veynante, Compressible large eddy simulation of turbulent combustion in complex geometry on unstructured meshes, Combustion and Flame 137 (2004) 489–505.

[14] E. Fernández-Tarrazo, A. L. Sánchez, A. Liñán, F. A. Williams, A simple one-step chemistry model for partially premixed hydrocarbon combustion, Combustion and Flame 147 (2006) 32–38.

[15] G. Boudier, L. Gicquel, T. Poinsot, Effects of mesh resolution on large eddy simulation of reacting flows in complex geometry combustors, Combustion and Flame 155 (2008) 196–214.

[16] B. Franzelli, E. Riber, M. Sanjosé, T. Poinsot, A two-step chemical scheme for kerosene–air premixed flames, Combustion and Flame 157 (2010) 1364–1373.

[17] W. Polifke, W. Geng, K. Döbbeling, Optimization of rate coefficients for simplified reaction mechanisms with genetic algorithms, Combustion and Flame 113 (1998) 119–134.

[18] B. Farcy, A. Abou-Taouk, L. Vervisch, P. Domingo, N. Perret, Two approaches of chemistry downsizing for simulating selective non catalytic reduction DeNOx process, Fuel 118 (2014) 291–299.

[19] D. A. Sheen, H. Wang, The method of uncertainty quantification and minimization using polynomial chaos expansions, Combustion and Flame 158 (2011) 2358–2374.

[20] A. S. Tomlin, T. Turányi, Investigation and improvement of reaction mechanisms using sensitivity analysis and optimization, Springer, 2013.

[21] J. Prager, H. N. Najm, K. Sargsyan, C. Safta, W. J. Pitz, Uncertainty quantification of reaction mechanisms accounting for correlations introduced by rate rules and fitted Arrhenius parameters, Combustion and flame 160 (2013) 1583–1593.

[22] M. Khalil, H. N. Najm, Probabilistic inference of reaction rate parameters from summary statistics, Combustion Theory and Modelling 22 (2018) 635–665.

[23] J. Bell, M. Day, J. Goodman, R. Grout, M. Morzfeld, A Bayesian approach to calibrating hydrogen flame kinetics using many experiments and parameters, Combustion and Flame 205 (2019) 305–315.

[24] F. vom Lehn, L. Cai, H. Pitsch, Sensitivity analysis, uncertainty quantification, and optimization for thermochemical properties in chemical kinetic combustion models, Proceedings of the Combustion Institute 37 (2019) 771–779.

[25] J. Wang, Z. Zhou, K. Lin, C. K. Law, B. Yang, Facilitating Bayesian analysis of combustion kinetic models with artificial neural network, Combustion and Flame 213 (2020) 87–97.

[26] W. Ji, Z. Ren, Y. Marzouk, C. K. Law, Quantifying kinetic uncertainty in turbulent combustion simulations using active subspaces, Proceedings of the Combustion Institute 37 (2019) 2175–2182.

[27] J. Li, Z. Zhao, A. Kazakov, F. L. Dryer, An updated comprehensive kinetic model of hydrogen combustion, International journal of chemical kinetics 36 (2004) 566–575.

[28] M. Khalil, G. Lacaze, J. C. Oefelein, H. N. Najm, Uncertainty quantification in les of a turbulent bluff-body stabilized flame, Proceedings of the Combustion Institute 35 (2015) 1147–1156.

[29] M. E. Mueller, V. Raman, Model form uncertainty quantification in turbulent combustion simulations: Peer models, Combustion and Flame 187 (2018) 137–146.

[30] M. E. Mueller, G. Iaccarino, H. Pitsch, Chemical kinetic uncertainty quantification for large eddy simulation of turbulent nonpremixed combustion, Proceedings of the Combustion Institute 34 (2013) 1299–1306.

[31] G. P. Smith, D. M. Golden, M. Frenklach, N. W. Moriarty, B. Eiteneer, M. Goldenberg, C. T. Bowman, R. K. Hanson, S. Song, W. C. Gardiner Jr, et al., Gri 3.0 mechanism, Gas Research Institute (http://www. me. berkeley. edu/gri_mech) (1999).

[32] A. Avdonin, S. Jaensch, C. F. Silva, M. Češnovar, W. Polifke, Uncertainty quantification and sensitivity analysis of thermoacoustic stability with non-intrusive polynomial chaos expansion, Combustion and Flame 189 (2018) 300–310.

[33] K. Zhang, X. Jiang, Uncertainty quantification of fuel variability effects on high hydrogen content syngas combustion, Fuel 257 (2019) 116111.

[34] B. Enderle, B. Rauch, F. Grimm, G. Eckel, M. Aigner, Non-intrusive uncertainty quantification in the simulation of turbulent spray combustion using polynomial chaos expansion: A case study, Combustion and Flame 213 (2020) 26–38.

[35] T. Turányi, Sensitivity analysis of complex kinetic systems. Tools and applications, Journal of mathematical chemistry 5

(1990) 203–248.

[36] H. Wang, D. A. Sheen, Combustion kinetic model uncertainty quantification, propagation and minimization, Progress in Energy and Combustion Science 47 (2015) 1–31.

[37] A. Roux, L. Gicquel, S. Reichstadt, N. Bertier, G. Staffelbach, F. Vuillot, T. Poinsot, Analysis of unsteady reacting flows and impact of chemistry description in Large Eddy Simulations of side-dump ramjet combustors, Combustion and flame 157 (2010) 176–191.

[38] C. K. Law, Combustion physics, Cambridge university press, 2010.

[39] T. Poinsot, D. Veynante, Theoretical and numerical combustion, RT Edwards, Inc., 2005.

[40] I. M. Sobol, Uniformly distributed sequences with an additional uniform property, USSR Computational Mathematics and Mathematical Physics 16 (1976) 236–242.

[41] R. G. Ghanem, S. D. Spanos, Stochastic Finite Elements: a Spectral Approach, Springer Verlag, 1991.

[42] O. Le Maître, O. M. Knio, Spectral Methods for Uncertainty Quantification, Scientific Computation, Springer, 2010.

[43] I. M. Sobol, Sensitivity estimates for nonlinear mathematical models, Mathematical modelling and computational experiments 1 (1993) 407–414.

[44] G. Kuczera, E. Parent, Monte Carlo assessment of parameter uncertainty in conceptual catchment models: the Metropolis algorithm, Journal of hydrology 211 (1998) 69–85.

[45] M. Akram, P. Saxena, S. Kumar, Laminar burning velocity of methane–air mixtures at elevated temperatures, Energy & Fuels 27 (2013) 3460–3466.

[46] Z. Liu, N. I. Kim, An assembled annular stepwise diverging tube for the measurement of laminar burning velocity and quenching distance, Combustion and flame 161 (2014) 1499–1506.

[47] Y. Lafay, B. Renou, G. Cabot, M. Boukhalfa, Experimental and numerical investigation of the effect of H2 enrichment on laminar methane–air flame thickness, Combustion and Flame 153 (2008) 540–561.

[48] A. Mazas, B. Fiorina, D. A. Lacoste, T. Schuller, Effects of water vapor addition on the laminar burning velocity of oxygen-enriched methane flames, Combustion and Flame 158 (2011) 2428–2440.

[49] M. C. Kennedy, A. O'Hagan, Bayesian calibration of computer models, Journal of the Royal Statistical Society: Series B (Statistical Methodology) 63 (2001) 425–464.

[50] M. C. Kennedy, A. O'Hagan, Supplementary details on Bayesian Calibration of Computer Models, Internal report (2001).

[51] D. Lucor, O. P. Le Maître, Cardiovascular modeling with adapted parametric inference, ESAIM: Proceedings and Surveys 62 (2018) 91–107.

[52] T. Poinsot, D. Veynante, S. Candel, Quenching processes and premixed turbulent combustion diagrams, Journal of Fluid Mechanics 228 (1991) 561–606.

[53] C. Meneveau, T. Poinsot, Stretching and quenching of flamelets in premixed turbulent combustion, Combustion and Flame 86 (1991) 311–332.

[54] M.-S. Wu, J. F. Driscoll, A numerical simulation of a vortex convected through a laminar premixed flame, Combustion and flame 91 (3-4) (1992) 310–322.

[55] W. L. Roberts, J. F. Driscoll, M. C. Drake, L. P. Goss, Images of the quenching of a flame by a vortex—to quantify regimes of turbulent combustion, Combustion and Flame 94 (1993) 58–69.

[56] C. J. Mueller, J. F. Driscoll, D. L. Reuss, M. C. Drake, M. E. Rosalik, Vorticity generation and attenuation as vortices convect through a premixed flame, Combustion and flame 112 (1998) 342–358.

[57] J.-M. Samaniego, T. Mantel, Fundamental mechanisms in premixed turbulent flame propagation via flame–vortex interactions: Part i: Experiment, Combustion and flame 118 (1999) 537–556.

[58] V. Moureau, P. Minot, H. Pitsch, C. Bérat, A ghost-fluid method for large-eddy simulations of premixed combustion in complex geometries, Journal of Computational Physics 221 (2007) 600–614.

[59] O. Colin, F. Ducros, D. Veynante, T. Poinsot, A thickened flame model for large eddy simulations of turbulent premixed combustion, Physics of fluids 12 (2000) 1843–1863.

[60] P. H. Renard, D. Thevenin, J. C. Rolon, S. Candel, Dynamics of flame/vortex interactions, Progress in energy and combustion science 26 (2000) 225–282.

[61] V. Moureau, P. Domingo, L. Vervisch, Design of a massively parallel CFD code for complex geometries, Comptes Rendus Mécanique 339 (2011) 141–148.